ISOTHERMAL SHAKEDOWN TESTS FOR THE 5×5 PRESSURIZED WATER REACTOR ROD BUNDLE IN THE AUTOMATED CRITICAL HEAT FLUX TEST FACILITY

A Thesis

by

CRAIG IVAN YOLANDA MENEZES

Submitted to the Office of Graduate and Professional Studies of
Texas A&M University
in partial fulfillment of the requirements for the degree of

MASTER OF SCIENCE

Chair of Committee,	Yassin A. Hassan
Co-Chair of Committee,	Rodolfo Vaghetto
Committee Member,	Maria King
Head of Department,	Michael Nastasi

December 2019

Major Subject: Nuclear Engineering

ABSTRACT

Pressurized water reactors employ rod bundles to generate thermal power via nuclear fission – which is extracted using water as the process fluid. Along the length of the rod arrangement, spacer grids are installed to increase turbulence and heat transfer rate. It is critical to estimate the temperature variations, pressure drop and frictional losses to obtain a better understanding of the efficiency and safe operation of a particular design used.

The TAMU CHF Facility is a complex experimental facility designed with the intent to study such operations. Development of such a facility is imperative to study thermal hydraulic parameters for specific fuel rod and spacer grid designs, and verify the results with computer modeled simulations.

The facility was upgraded to facilitate automation, remote operation, acquisition of high-fidelity experimental data and analysis. Subsequently, temperature changes, pressure and flow related parameters were estimated at various Reynolds numbers for specified increments in loop pressure, using water as the process fluid.

ACKNOWLEDGEMENTS

I would like to thank my committee chair, Dr. Yassin A. Hassan, and my committee co-chair, Dr. Rodolfo Vaghetto, for providing the opportunity to pursue the research at the Thermal Hydraulic Research Laboratory – over the course of my degree program. Their guidance, assistance and support throughout the program has been extremely beneficial towards my professional development. I would like to thank my committee member, Dr. Maria King, for her patience, support and valuable input.

Special thanks to Mr. William Headley for his continual assistance – even at odd hours – in the research carried out at the CHF Facility; as well as helping me get familiar with many aspects of facility construction, fittings and engineering design. I would also like to acknowledge the assistance and technical support of Mr. Timothy Triplett and Mr. Greg Rose from Coherent Technologies, Inc., related to the complex process control systems which I have worked on. Thanks to Mr. Chris Wilbur for his assistance in the reconstruction and operation of the CHF facility, after acquisition by the THR Laboratory.

I would like to thank my mother, Mrs. Yolanda Menezes, for her unwavering support throughout my academic ventures. I am also grateful for my aunt, Mrs. Philomena Toor and my uncle, Mr. Fabian D'Souza, for their motivation and assistance. Finally, I would like to thank Ms. Sharlyn D'Souza for being a strong support structure and motivating me through my academic journey.

CONTRIBUTORS AND FUNDING SOURCES

Contributors

This work was supervised by a thesis committee consisting of Dr. Yassin A. Hassan and Dr. Rodolfo Vaghetto of the Department of Nuclear Engineering and Dr. Maria King of the Department of Biological and Agricultural Engineering.

The facility construction from ground zero, systems communication and connections were performed by Mr. William Headley, from the Department of Nuclear Engineering. The facility was also constructed with the assistance of Mr. Chris Wilbur and the student researchers at the Thermal Hydraulic Research Laboratory at Texas A&M University.

The preliminary designs in Ignition 7.9 and the logic trees by which the facility operates were constructed by Mr. Timothy Triplett and Mr. Greg Rose of Coherent Technologies, Inc.

All other work conducted for the thesis was completed by the student independently.

Funding Sources

Graduate study was supported by assistantship from the Department of Nuclear Engineering at Texas A&M University.

NOMENCLATURE

A_{CS}	Flow Cross Sectional Area
AC	Alternating Current
ASME	American Society of Mechanical Engineers
BWR	Boiling Water Reactor
CHF	Critical Heat Flux
D_H	Hydraulic Diameter
DAQ	Data Acquisition System
DC	Direct Current
DI	De-Ionized
DIN	Deutsches Institut für Normung
DNB	Departure from Nucleate Boiling
DNBR	Departure from Nucleate Boiling Ratio
DP	Differential Pressure
IDE	Integrated Development Environment
f	Darcy Friction Factor
K	Spacer Grid Loss Coefficient
L	Flow Characteristic Length
MV	Mixing Vane
n	Number of Spacer Grids
NI	National Instruments

P	Pressure
P	Perimeter
PFA	Perfluoro alkoxy
PLC	Programmable Logic Controller
PVC	Polyvinyl Chloride
PWR	Pressurized Water Reactor
Q	Volumetric Flow Rate
Re	Reynolds Number
RTD	Resistance Temperature Detector
SCADA	Supervisory Control And Data Acquisition
SS	Stainless Steel
S-S	Simple Spacer
TAMU	Texas A&M University
T	Temperature
TC	Thermocouple
UI	User Interface
v	Fluid Velocity
VFD	Variable Frequency Drive
ρ	Fluid Density
μ	Fluid Dynamic Viscosity
ν	Fluid Kinematic Viscosity
σ	Standard Deviation

TABLE OF CONTENTS

Page

LIST OF FIGURES

Page

Page

Page

LIST OF TABLES

Page

1. INTRODUCTION

1.1. Importance of the TAMU CHF Facility

The TAMU Critical Heat Flux test loop provides a means of evaluating the departure from nucleate boiling performance of test geometries representative of commercial pressurized water reactor nuclear fuel. The rod bundle within the test section, with DC power heating, will be used to closely replicate traditional nuclear fuel rods. This would enable the study of heat transfer and fluid flow behavior, similar to designs used in PWRs currently in operation or being tested. It is imperative to have knowledge of the critical heat flux and bundle pressure drop values, with sufficient confidence for a particular nuclear fuel design. Since pressurized water reactors are going to be operational for the foreseeable future, increasing their operational efficiency is the best course of action, when it comes to upgrading an existing fuel design. The parameters such as critical heat flux and spacer grid loss coefficients are typically found only via experimental procedures and correlations, due to their complex dependence on a variety of phenomena. The TAMU CHF loop can be used as a platform for which the relevant thermal hydraulic parameters can be measured, for existing and newer fuel designs. This would allow for an inherent increase in operational efficiency and safety – which are both critical to any reactor design.

1.2. Boiling and CHF Phenomena*

Boiling phenomena displays the distinct variation between various boiling regimes [1]. These regimes are characterized by the rate, shape and size of vapor bubbles emerging from the heated surface. Figure 1.1. shows the boiling curve for water at 1 atm. This curve was first generated by the experiments performed by Nukiyama, with a simple pool boiling apparatus consisting of a nichrome heating wire. It should be noted that the temperature scale displays ΔT_{excess}, which is the available temperature – the difference between the heater wall temperature and the bulk fluid temperature.

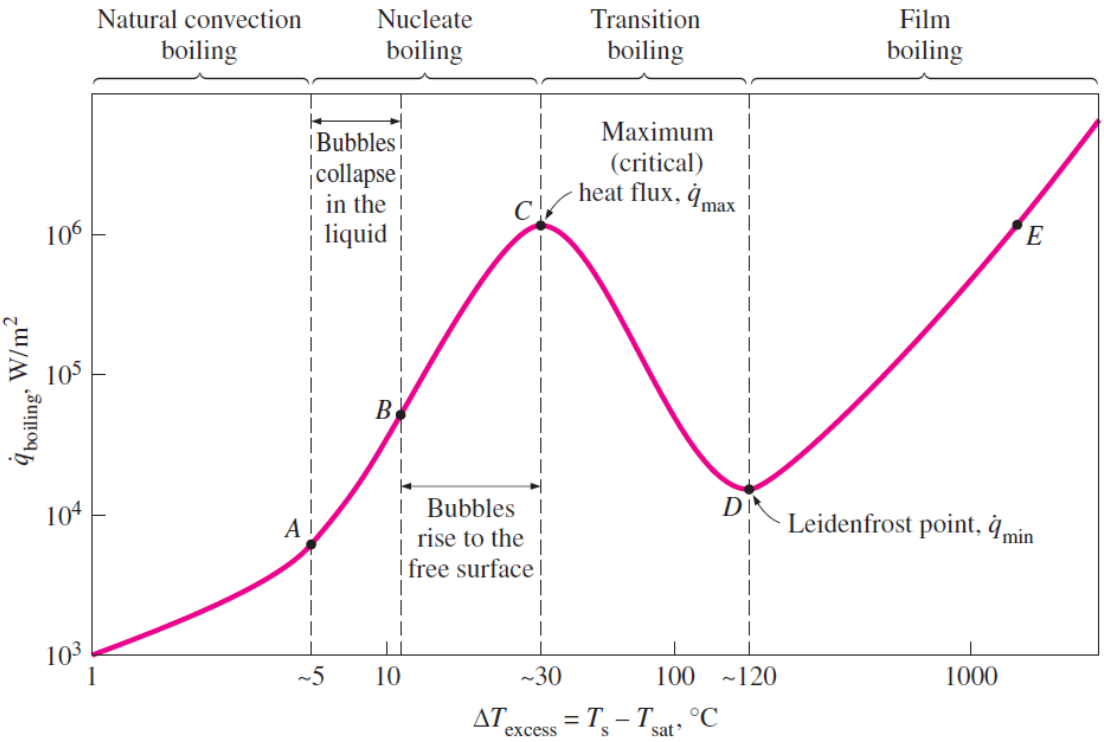

Figure 1.1. Boiling regimes for water at 1 atm (Reprinted from [1]).

* Part of the theory in this chapter is adapted from '*Introduction to Thermodynamics and Heat Transfer, 2nd Edition*', Cengel, Yunus A., 2009, McGraw-Hill Higher Education, Copyright 2009.

As seen in Figure 1.1., the nucleate boiling regime can be separated into two distinctly identifiable regions. In region A–B, isolated bubbles are formed at various nucleation sites on the heated surface which dissipate in the liquid shortly after they separate from the surface. As the heater temperature is further increased in region B–C, bubbles form rapidly giving rise to numerous seamless columns of vapor in the liquid. The combined effect of liquid entrainment and evaporation lead to large heat fluxes in the system.

As the heater temperature and thus the ΔT_{excess} is increased past point C, the heat flux decreases, as shown in Figure 1.1. This is because a large fraction of the heater surface is covered by a vapor film, which acts as an insulation due to the low thermal conductivity of the vapor relative to that of the liquid. In the transition boiling regime, both nucleate and film boiling partially occur. Nucleate boiling at point C is completely replaced by film boiling at point D. Operation in the transition boiling regime, which is also called the unstable film boiling regime, is avoided in practice.

In both PWRs and BWRs, the problem is more or less associated with departure from nucleate boiling. The nucleate boiling heat flux cannot be increased indefinitely. At the maximum or the critical heat flux value, the steam produced forms an insulating blanket over the surface, leading to a deterioration in the heat transfer coefficient between the rods and the process liquid. Immediately after the critical heat flux has been reached, boiling becomes unstable and film boiling occurs. The transition from nucleate boiling to film boiling is known as the ‘boiling crisis’. The CHF phenomena causing the deterioration of heat transfer are different for PWRs and for BWRs, due to their differing

operating conditions. The boiling crisis in BWRs includes dryout in the high-quality region, whereas in PWRs, the departure from nucleate boiling occurs in the subcooled or low-quality region. But the critical heat flux is used for both regimes.

For PWRs, the critical safety issue is named Departure from Nucleate Boiling (DNB). The formation of a local vapor layer occurs, causing a considerable reduction in heat transfer. This phenomenon is primarily observed in the subcooled region. The behavior of the boiling crisis depends on many thermal hydraulic parameters such as pressure, temperature, flow rate; but the boiling crisis occurs at a relatively high heat fluxes. This appears to be associated with the cloud of bubbles neighboring the surface. These bubbles or film of vapor reduces the amount of incoming water causing a deterioration in the heat transfer coefficient. As the heat flux remains, the heat then accumulates in the fuel rod, having no other medium for heat transfer, causing the spikes in the cladding and fuel temperature. This very high temperature difference is required to transfer the critical heat flux being produced from the surface of the fuel rod to the reactor coolant via the encompassing vapor blanket.

Additionally, in case of PWRs, the critical flow is inverted annular single phase flow, while in BWRs, the coolant flow is usually two-phase annular flow. A key safety requirement is that DNB will not occur during steady state operation, normal operational transients and anticipated operational occurrences. Fuel cladding integrity will be preserved if the minimum DNBR remains above the 95/95 DNBR limit for PWRs – 95% probability at a 95% confidence level. DNB criterion is one of acceptance criteria in

nuclear reactor safety analyses since it constitutes one of safety limits in technical specifications for mechanical design.

One of the most widely used design correlations for predicting departure from nucleate boiling is the W-3 correlation developed by Tong, at the Westinghouse Atomic Power Division. It is applicable for subcooled regime and for low to moderate quality flows. The W-3 correlation is a function of coolant enthalpy considering the saturated and inlet conditions, pressure, quality and coolant mass flux. Alternatively, CHF look-up tables are also used widely for the prediction of the critical heat flux. A CHF look-up table is fundamentally a standardized data bank for a vertical 8 mm water-cooled tube.

1.3. Pressure Drop and Grid Loss Coefficients*

In general, total fuel assembly pressure drop constitutes of the fuel bundle frictional pressure drop – which depends on the relative roughness of fuel rods, Reynolds number, hydraulic diameter and characteristic flow length of the rod [2]. The other pressure drops include that of structural elements such as the top and bottom nozzle, spacer grids or mixing vane grids. It is convoluted to analytically estimate pressure drops in fuel assemblies due to the complex flow patterns associated with these structures. Therefore, pressure drops are measured in experimental hydraulic loops, rather than analytically calculated – due to the uncertainty in the flow patterns.

* Part of the theory in this chapter is adapted from '*Nuclear Systems I - Thermal Hydraulic Fundamentals*', Todreas, Neil E.; Kazimi, Mujid S., 1990, Taylor & Francis Group, Copyright 1990.

Usually, the pressure loss coefficient, K, is used for minor losses in pressure head. This coefficient characterizes pressure loss of a specific hydraulic system or a part of a hydraulic system. The pressure loss coefficient can be defined and measured for both straight pipes and rod bundles.

The Darcy friction factor – a dimensionless quantity used in the Darcy – Weisbach equation, is historically used for the description of frictional losses in pipe or duct as well as for open-channel flow. This is also called the Darcy – Weisbach friction factor, or simply friction factor.

The friction factor depends on the Reynolds number for the flow in addition to the degree of roughness of the pipe's inner surface. This is true especially for flow in the turbulent regime. On the other hand, in the laminar flow regime, the friction factor is independent of roughness of the pipe's inner surface.

The pipe cross-sectional area is also important, since deviations from circular cross-section will cause secondary contributing to the increase in pressure head loss. Non-circular pipes and ducts are treated using the hydraulic diameter (D_H). As an illustration, for a hydraulically smooth pipe with fluid flowing in the turbulent flow regime, the friction factor can be approximated by Blasius formula [3] stated below.

$$f = 0.316\,Re^{-0.25}$$

An important factor to consider is that at very large Reynolds numbers, the friction factor is independent of the Re. This is due to the thickness of laminar sublayer decreasing with increasing Re. For very large Re the thickness of laminar sublayer is equivalent to the surface roughness and which directly influences the flow. The laminar

sublayer becomes so fine that the surface roughness protrudes into the flow layer. In this situation, the frictional losses are produced in the main flow primarily by the protruding roughness elements, and the contribution of the laminar sublayer is negligible.

1.4. Other Critical Heat Flux Test Facilities

Texas A&M University's Critical Heat Flux Test Facility is one of multiple thermal hydraulic test facilities around the world studying thermal hydraulic parameters under extreme test conditions. The capabilities of similar test facilities include the ability to study single phase flow patterns, pressure losses, near accident conditions and fuel components testing. These are essential for the understanding of PWRs and newer designs that improve upon the existing PWR design prototypes. Additionally, test facilities also include the study of dryout in prototypical BWR rod bundles. Two phase flow regimes and behavior are important topics for research in such designs. All of these facilities also study the effects of spacer grids on pressure differential, frictional losses and turbulence induced in their vicinity.

Westinghouse Electric Co. engineered their ODEN test facility in Vasteras, Sweden to study PWR designs [4]. This facility possesses the capability to house a 5×5 or a 6×6 prototypical full length PWR rod bundle. The ODEN Loop can operate up to 12 MW of DC heating and to a maximum pressure of 20 MPa. Westinghouse also operates their FRIGG Facility in Vasteras, Sweden, to study dryout in BWR rod bundles [5]. This facility has the capability to operate at 15 MW, 10 MPa for a full length 8×8 or 11×11 BWR fuel bundle. Similarly,

AREVA designed a test facility to study both PWR and BWR fuel bundle performance, in Karlstein, Germany [6]. This is the KATHY facility with the maximum operating limits at 20 MW and 16.5 MPa – for either a 7×7 GAIA design PWR bundle or a full scale BWR Bundle. The University of Wisconsin at Madison (UW-M) in collaboration with Oregon State University (OSU), have an experimental set-up called the 'High Pressure Critical Heat Flux Facility (HPCHF) for high pressure and low mass flux regimes for a 2×2 rod bundle [7]. Table 1.1. summarizes these experimental facilities and their operational capabilities.

Table 1.1. Summary of select experimental test facilities researching CHF and dryout.

Sr. No.	Facility	Location	Rod Assembly	Maximum Power (MW)	Maximum Pressure (MPa)
1	TAMU CHF Test Facility	College Station, U.S.A.	5×5 PWR	0.5	2.8
2	Westinghouse - ODEN	Vasteras, Sweden	5×5 PWR 6×6 PWR	12	20
3	Westinghouse - FRIGG	Vasteras, Sweden	8×8 PWR 11×11 PWR	15	10
4	AREVA - KATHY	Karlstein, Germany	7×7 PWR 8×8 BWR	20	16.5
5	UW-M, OSU - HPCHF	Madison, U.S.A.	2×2 PWR	0.1	16

1.5. Project Scope

As seen in the preceding sections, it is imperative to determine the complex thermal hydraulic parameters and correlations for specific fuel designs. In this research, the TAMU CHF loop was upgraded to achieve high-fidelity data to aid in experimentation related to nuclear fuel designs. Operational automation was configured so that pressures, flow rates and temperatures can be observed and used for further experiments. All sensors were calibrated and verified for accuracy, for high reliability of data during testing. System parameter control was achieved by means of using high gain control valves, for quick responses to perturbations in process variables, such as the temperature and pressure of the system. Varying pressure tests at isothermal conditions were carried out to confirm the grid loss coefficients and to obtain thermal hydraulic parameter trends. These results were then compared to literature to observe the repeatability of data and to ensure complete experimental operation.

2. FACILITY DESCRIPTION

The TAMU Critical Heat Flux Test Facility (Figure 2.1.) was previously operated by Westinghouse Electric Co. for CHF experimentation [8]. It includes a test vessel, piping and process fluid flow system, process control system, electrical power supply units, various instrumentation for desired parameters, data acquisition system and display units. The test section was constructed in accordance to ASME section VIII, Division I using SS-304. It is rated for a maximum pressure of 400°F. The maximum allowable flow rate is 15.699 kg/s. The vessel internals have the capacity to house 7×7 rod bundles. Currently, 5×5 rods are used with prototypical Westinghouse spacers cut from a typical 17×17 spacer grid - which are commonly used in commercial nuclear reactors. The entire test section has insulation to minimize heat losses and to assist in the overall energy balance.

Figure 2.1. TAMU CHF test facility with all components installed.

2.1. Flow Pattern

Upon entrance via the inlet to the test section, the process fluid would flow downwards through the test section, outside the duct housing the rod bundle and is then forced into the duct flowing upwards through the rods. The overall flow diagram is seen in Figure 2.2.

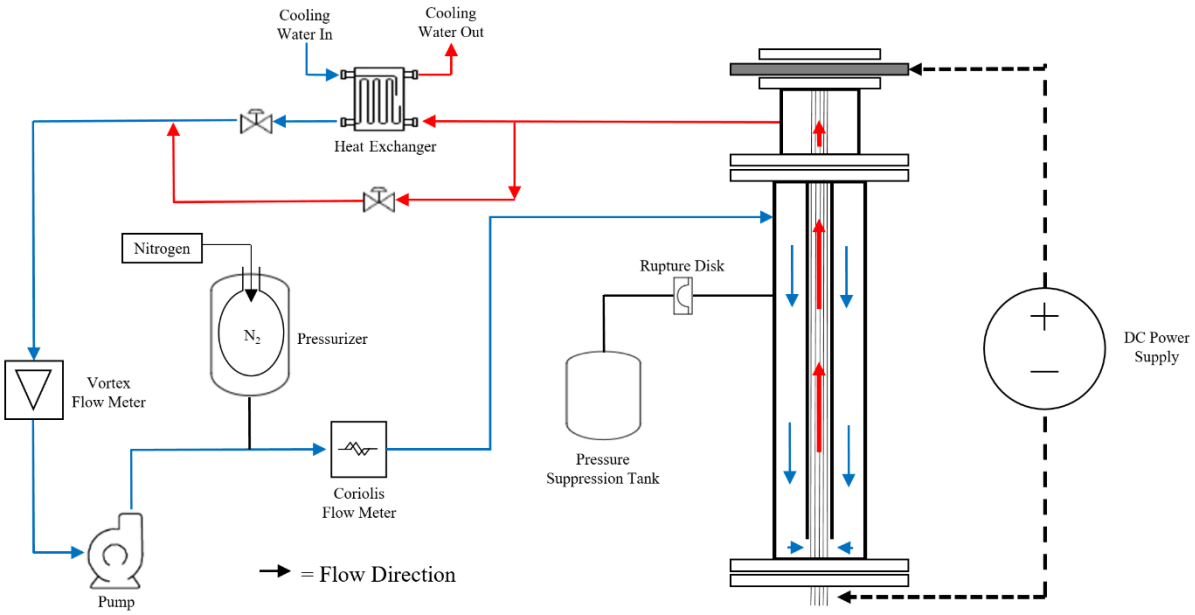

Figure 2.2. CHF loop flow diagram displaying all installed components.

2.2. Test Section Internals

The internal components of the test section include a flow distributor, a shroud box, ceramic and non-ceramic flow liners. The flow distributor collects flow incoming from the downcomer and evenly distributes the process fluid. The shroud box is a rigid SS housing which contains the flow liners and the rod bundle. To make sure that the flow geometry remains intact, ceramic flow liners constructed from Al_2O_3 were used. It consists of pressure tap holes at specific locations to monitor the differential pressure.

Subsequently, non-ceramic flow liners were fit into the flow channel upstream of the ceramic flow liners to minimize flow disturbance.

2.3. Rod Bundle

The rod bundle is made up of the heater rods and grid spacers. Each rod consists of an 80 inch heated Inconel tube section, two 10 inch unheated nickel sections upstream and downstream, respectively. All the three sections were brazed together as a single rod. K-type thermocouples were installed at two locations at the upper end of each rod - as seen in Figure 2.3. – to detect the DNB condition. Figure 2.3. also shows the locations of the pressure taps used to measure differential pressure.

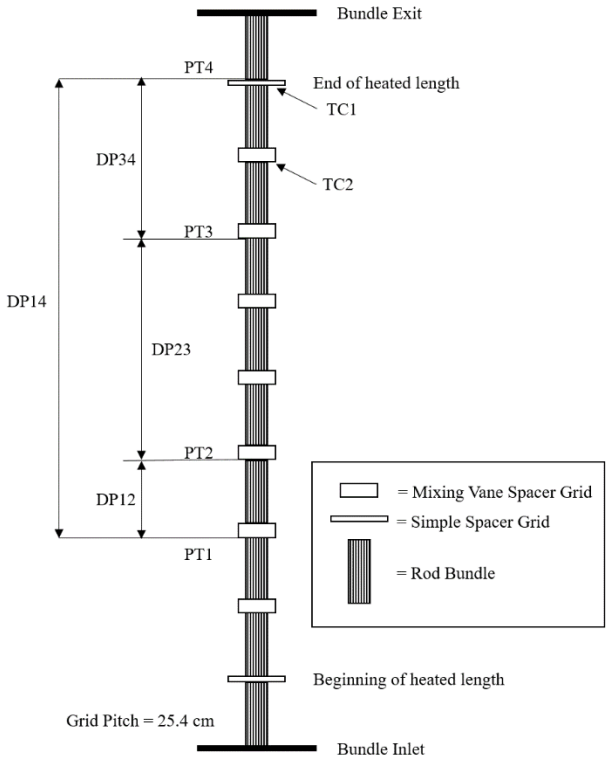

Figure 2.3. Rod bundle schematic with the location of SS grids, MV grids, differential pressure taps and thermocouples (Reprinted from [8]).

The pressure taps are SS rods that penetrate through the test section and the ceramic flow liner, to allow access for differential pressure measurement. Al_2O_3 ceramic tubes were utilized to electrically shield the thermocouple wires and brazed junctions from the electrically powered Inconel and nickel tube sections to dissuade any electrical interference.

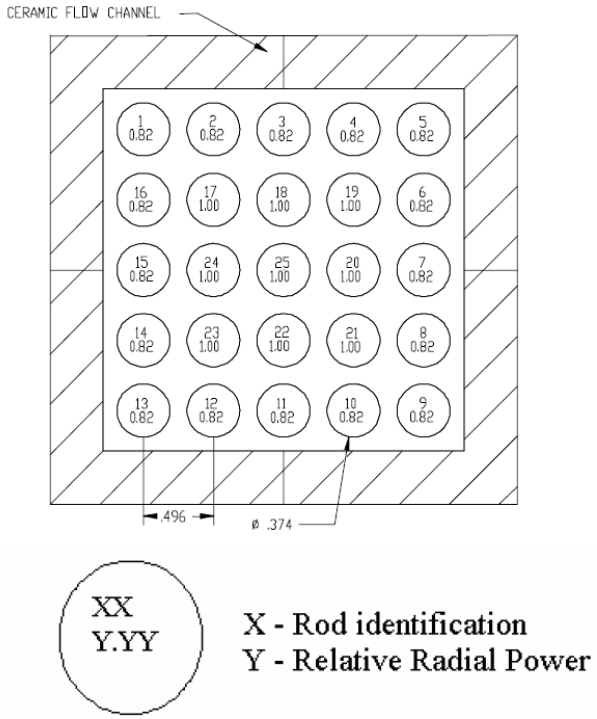

Figure 2.4. Heated tubes within the ceramic flow liner showing the rod identification number and the relative radial power (Reprinted from [8]).

The tubes are numbered as seen in Figure 2.4. The 9 center tubes with numbers 17 to 25 were constructed from Inconel 600 and operate at 100% electrical power. The peripheral heated tubes, numbered 1 to 16 operate at approximately 82% of the supplied electrical power. Turbulence is induced by the MV grids (Figure 2.5.) which benefits

forced heat transfer by increasing the localized Reynolds number. These mixing vane grids are present at 7 locations equidistantly spaced from each other.

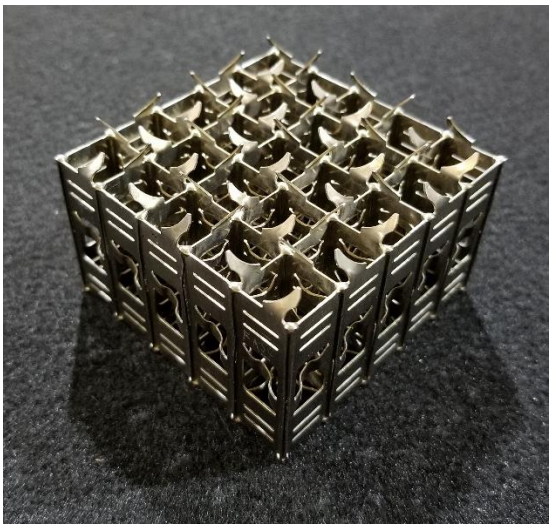

Figure 2.5. 5×5 prototypical PWR spacer grid installed in the rod bundle.

Additionally, 2 S-S grids are installed at the upper and lower extremities of the rod heated lengths. These grids are positioned to maintain the geometry of the heated rods. They also perform the function of minimizing rod bowing arising from electromagnetic forces as well as the effect of flow induced vibrations. Both the S-S and MV grids consist of springs to minimize flow induced vibrations and to facilitate slight movement in the rods without any damage to the rod geometry. The complete rod assembly is observed in Figure 2.6.

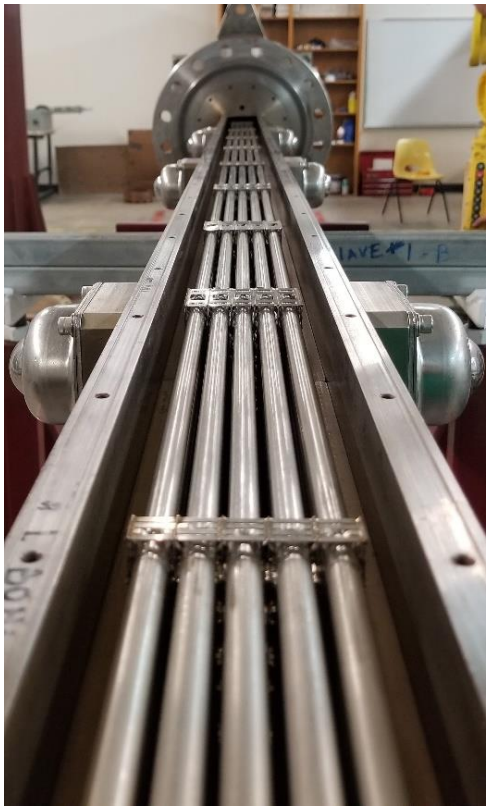

Figure 2.6. Rod bundle in flow duct, with spacer grids and mixing vanes.

2.4. Electrical Power Supply

3 Robicon transformers, shown in Figure 2.7., were utilized to convert 480 V AC current to DC current which is to be supplied to the test section. The Robicon units consist of one 'Master' unit and two 'Slave' units. Each provide a 60 V, 4200 A output – for a combined output of 60 V, 12600 A and a maximum power of 756 kW. It is interesting to note that the power supply was limited to 500 kW to protect the power cables from damage. Each Robicon unit is cooled by a 2-inch city tap water supply, to prevent overheating during operation.

Figure 2.7. Robicon transformers used to convert AC to DC - to electrically heat the rods within the test section.

A maximum power of 500 kW can be achieved in the CHF test loop via the DC powered heating system. 12 2-inch power cables were attached to a copper plate at the bottom of the test section, connected directly to the Robicon transformers. A copper cup containing – which is a low melt alloy was used to provide an electrically seamless connection from the copper housing to the unheated electrically conductive segment of the rods. A specialized mobile cart had to be used to lift the copper housing parts since they weigh in excess of 50 lbs., while also being able to access the fairly limited space below the test section. Additionally, 12 2-inch cables were connected at the upper electrically conductive plate, to complete the circuit.

2.5. Heat Removal

To extract process heat, a 1 MW brazed plate heat exchanger (Figure 2.8.) was installed. This heat exchanger is operated using city tap water in conjunction with a forced convection air-cooled cooling tower. The cooling tower which rejects heat to the surroundings is located external to the facility premises. A bypass process fluid line was installed with the idea of use in process control. When the cooling tower is not in operation, all process fluid is bypassed by means of flow channeling with control valves.

Figure 2.8. Brazed plate heat exchanger which will operate using city water supply.

2.6. Flow Regulation

The loop has a 40 HP magnetically coupled centrifugal pump, shown in Figure 2.9., installed to achieve the desired flow rate. The pump is operated using a VFD comprising of an AC motor – which goes up to 60 Hz – a drive controller and a drive interface. The specifications of the pump include a rating of 250 gallons/min to provide a 225 ft head. It also possesses low leakage characteristics to prevent the process fluid from accidentally exiting the flow system.

Figure 2.9. 40 HP pump used in the facility coupled to a VFD to regulate the flow rate.

2.7. Facility Pressurization

System pressurization is achieved using a 40 gallon surge suppressor tank, also referred to as the pressurizer, displayed in Figure 2.10. The pressurizer is of the bladder type with a nitrile-based bladder installed internally. The pressurizer performs two functions in the test loop. Primarily, on inflating or deflating the bladder using high-

pressure nitrogen (N_2) gas, the system can be pressurized or depressurized, respectively. The process fluid occupies the space external to the bladder within the surge suppressor tank – directly connected to the flow loop. Additionally, the pressurizer also protects the system from accidental pressure surges. To protect the system from accidental over pressurization, the test section is connected to a 550 psid suppression disc routed to another 20 gallon pressure suppression dome. If the system pressure exceeds the rating of the suppression disc, the disc will rupture allowing excess system fluid to drain into the suppression dome. Another means of pressurization and leak prevention was achieved using N_2 lines connected to the top and the bottom of the test section, via high pressure N_2 gas lines used by the pressurizer.

Figure 2.10. Surge suppressor tank with Nitrogen-filled bladder to pressurize the process fluid in the CHF facility.

3. INSTRUMENTATION, MEASUREMENT AND UPGRADES

The primary parameters of interest that are required to be measured by the Critical Heat Flux test loop are loop flow rate, inlet and outlet temperatures of the tests section, differential pressure at various points along the rod bundle and total power input. Temperatures at various sections in the loop are also required to be measured for safe operation and process control. The following subsections describe the instrumentation used for the aforementioned thermal hydraulic parameters associated with the CHF loop.

3.1. Data Acquisition System

The primary interface for acquiring all parameters is the NI DAQ system connected to a desktop computer in the vicinity of the CHF loop. The DAQ cards and their uses are shown in Table 3.1. All instrumentation can be found in Appendix A to D.

Table 3.1. DAQ card information and their connections to the main chassis.

Component	Model No.	Chassis Slot No.
Data Acquisition System	PXIe-1078	-
PXIe Cable Slot	-	1
8 Ch Bridge Input	HY5005-2	2
32 Ch Thermocouple Analog Input	TB-4353	3
	TB-4353	4
	TB-4353	5
	TB-4353	6
32 Ch Filtered Analog Input (Pressure and Flow)	TB-4302C	7
(Empty)	-	8
20 Ch RTD Input	TB-4357	9

The DAQ system has various cards attached, for each parameter to be measured, based on acquisition and hardware requirements. It is important to note that each card had to be synchronized to the same sample rate and sample frequency to avoid errors in data logging.

3.2. Temperature Measurement

The thermocouples were connected to the DAQ using PFA insulated thermocouple wire of the same specifications as required by the K-type thermocouples. The wire material used matched the thermocouple material – Chromel for the positive lead and Alumel for the negative terminal. Similarly, sheathed and PFA coated 4-wire RTD cable were used for each of the 4 RTD probes.

All temperature sensors were routed to the DAQ using a combination of steel and PVC tubing to conceal the wires and to prevent accidental damage to the long lengths of lead wires. The RTDs and thermocouples were connected to the DAQ cards and the connections were duly tested.

3.2.1. Loop Temperature Measurement

For the purposes of monitoring the temperature at various points in the loop, a combination of K-type thermocouples (range: 0 to 700°C) and 4-wire Pt-100 RTDs (range: -12 to 450°C) were employed. The locations of each sensor are shown in Table 3.2. The group numbers in the table indicate the coupling of sensors used for calibration, due to their proximity, for multiple calibrations at one point of time.

Table 3.2. Temperature sensor locations at various points in the CHF facility.

Group	Label	Sensor Type	Location
1	TE5810 C	RTD	Test Section Bottom
	TE5810 D	TC	Test Section Bottom
	TE5810 E	TC	Low Melt Heater
2	TE5809 A In	TC	Robicon Slave #1 Water Supply Inlet
	TE5809 A Out	TC	Robicon Slave #1 Water Supply Outlet
3	TE5809 B In	TC	Robicon Master Water Supply Inlet
	TE5809 B Out	TC	Robicon Master Water Supply Outlet
	TE5809 C In	TC	Robicon Slave #2 Water Supply Inlet
	TE5809 C Out	TC	Robicon Slave #2 Water Supply Outlet
4	TE5808 A	TC	Heat Exchanger Outlet
	TE5810 A	TC	Pump Upstream
	TE5810 G	RTD	Pump Downstream
5	TE5810 B	RTD	Test Section Inlet
	TE5808 B	RTD	Heat Exchanger Inlet
	TE5810 F	TC	Test Section Outlet

2 K-type thermocouples were also installed per Robicon transformer, at each inlet and outlet of the cooling water supply – to monitor the variation of the temperature in the transformers when DC power heating is utilized.

RTDs with a 1/10 DIN, Class A certified accuracy were selected for the inlet and outlet of the test section and the heat exchanger, respectively. The motivation behind the choice of these temperature sensors was to ensure high accuracy and excellent sensitivity subsequently positively affecting the loop process control. A higher confidence in data for post processing is also ensured with these sensors.

3.2.2. Rod Temperature Measurement

At the end of the heated section of the rods, 4 thermocouples per rod (barring two) were installed to study the Critical Heat Flux phenomena – since the maximum temperatures are skewed towards the upper segment of the test section. A total of 98 thermocouples were used to monitor the local temperature in this section. These thermocouples were labeled appropriately based on their location and then routed to the DAQ using the PVC pipe. Figure 3.1. shows the connections coming from the test section. Appendix E gives the rod thermocouple location and their connection to the DAQ.

Figure 3.1. Axial rod thermocouples routed to the DAQ from the test section.

3.2.3. Temperature Sensor Calibration

RTDs and TCs are calibrated using the same method, as described below. Calibration for the RTDs and TCs primarily consist of three steps:

1. Correct positioning of the temperature sensors and Initial Set-up.
2. Record steady-state data for 3 set-points that span the system's operating range.
3. Form a correction curve for each temperature sensor by evaluating reference measurement data vs. uncalibrated instrument data.

3.2.3.1. Calibration Set-up

The required equipment used consists of the system of probes, lead wires and the DAQ. A LabVIEW 2018 interface was created to record data. Reference measurements were logged with a Fluke 1524 Thermometer connected to a Fluke 5615 reference RTD probe – with an accuracy of 0.015°C.

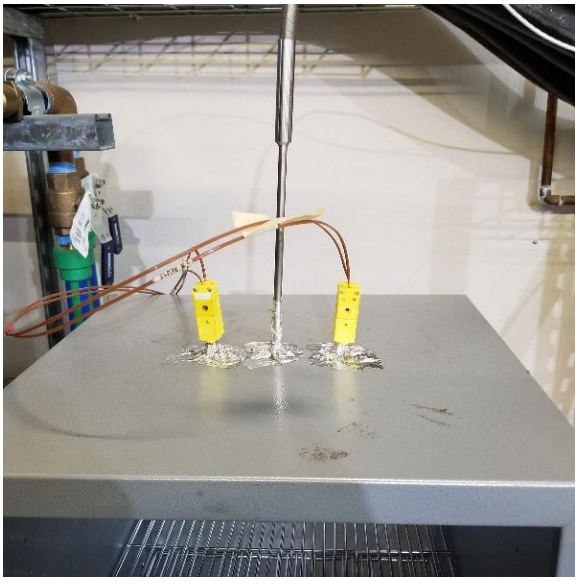

Figure 3.2. Thermocouple sensors positioned in the oven using aluminum tape.

The temperature sensor probes were placed in the slots on the upper over wall and positioned using aluminum tape (Fig. 3.2.). The probes were placed as close as possible, to each other – to ensure a maximum elimination of internal gradients within the oven. Such gradients arise from the heater constantly switching on and off to maintain steady state as well as heat losses from the walls of the oven. Placing the ends of the probes on a similar plane (possibly tilted towards the reference probe), as shown in Figure 3.3., reduces discrepancies caused due to temperature gradients.

Figure 3.3. Closest approachable positioning distance between the reference probe (center) and the uncalibrated temperature sensors.

Calibration at room temperature was performed using a ceramic insulation pouch (Fig. 3.4.). The pouch and probes were left overnight or approximately 12 hours to stabilize to room temperature. For high temperature data points, the oven was switched on and adjusted to the desired set point, and allowed to attain the corresponding steady-state temperature. This step generally takes around 4 hours or longer.

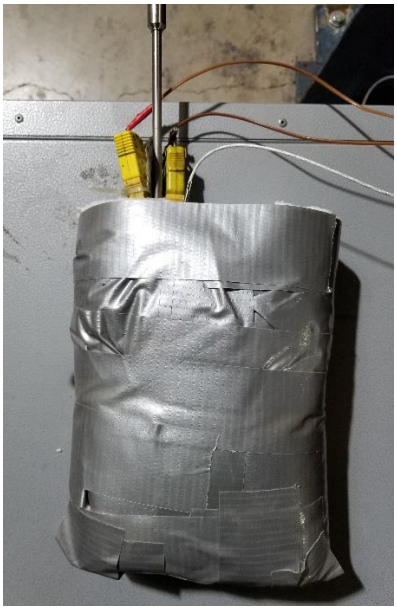

Figure 3.4. Ceramic insulation pouch used to collect steady-state room temperature data.

The LabVIEW interface is configured to record temperature data at 1 Hz for a time period of 300 seconds (5 minutes). The individual thermocouples were configured appropriately by selecting the channel, the correct thermocouple type (K-type) and temperature range. Similarly, the RTDs were initialized by selecting the channel, type (4 wire, Pt 3851) and temperature range.

3.2.3.2. Recording Measurements

The RTD and Thermocouple sensors were calibrated using three points – Room Temperature (~20°C, ~130°C and ~220°C) spanning the range of the CHF Test Facility (25–205°C). It should be noted that both these sensors have a linear response. The sensors were grouped according to their position in the CHF loop to allow multiple readings.

The stabilization time to steady state varies depending on the set point temperature, although a time period of approximately 4 hours is sufficient. A constant standard deviation implies that there is little variation in the spread of data. Constant or steady-state standard deviations for $\sigma < 0.6°C$ are acceptable to begin acquiring data points.

The readings from the uncalibrated sensors were acquired and organized for post-processing using Microsoft Excel. To account for the alternating changes in heating, average temperature values over the data accumulation period were used. Simultaneously, the reference probe was manually set to acquire the average temperature for the same start and end period as the uncalibrated probes.

3.2.3.3. Generating and Applying Calibration Curves

The average temperature values and standard deviation for the uncalibrated probes were utilized to create a calibration curve unique to the individual temperature sensors. The averaged data values were then added to the NI Max interface to display the calibrated temperatures. To encompass temperatures outside the range, extrapolated data using the trend line equation, at 0°C and 250°C, were also added in NI Max calibration curve. Since a linear fit is selected based on the response of the sensors, the equation $y = mx + c$ was used. This was performed in case the temperatures drop or exceed the calibration limits. All calibration data can be viewed in Appendix F.

3.3. Pressure Measurement

Rosemount 2051 pressure transmitters are located at various locations to monitor system pressure. Table 3.3. displays the location of the pressure transmitters and their corresponding connection to the DAQ. Figure 3.5. shows the pressure transducer grid with the SS pressure tubing which run along the facility supports to the positions of interest.

Figure 3.5. Pressure transducer grid – differential and gauge – connected to various points along the CHF facility.

Absolute pressure measurements at the inlet and the outlet give the test section pressure drop. It should also be noted that the maximum occurring pressure occurs at the discharge of the pump. Correspondingly, 4 differential pressure measurements via DP

pressure transducers are utilized in the test section. The zones are shown in the Figure 2.3. (along with rod thermocouples). All loop pressure data was obtained in psi whereas the differential pressure data obtained was in inches of H_2O. Differential pressure measurements are carried out to observe grid pressure drops and to make sure that the bundle geometry remains intact during facility operation. The locations of all pressure transducers are given in Table 3.3.

Table 3.3. Pressure transducer locations in the CHF Facility.

Sr. No.	Pressure Transducer Label	Location
1	PDT5810 D	DP 12
2	PT5810 A	N2
3	PT5810 B	Pump
4	PDT5810 E	DP 23
5	PT5810 H	Bundle Exit 1
6	PDT5810 G	DP 13
7	PDT5810 F	DP 34
8	PDT5810 K	Bundle Exit 2
9	PT5810 C	Inlet
10	PT5810 J	Outlet

Pressure fittings were installed at each port to ensure sustainability of transmitters and minimal leakage of process fluid at higher operating pressures. The pressure transducers operate such that they receive power and transmit an output between 4 to 20 mA, from the DAQ. CAT 6 Ethernet cable was used to complete these connections. 4 mA output corresponds to the minimum recorded temperature (in most cases 0 psia) whereas 20 mA corresponds to the maximum pressure recordable.

3.3.1. Pressure Transmitter Calibration

The calibration of these pressure transducers was performed after shipping it to the Calibration Division of Fluke Instruments and the corresponding calibration curves were applied to the LabVIEW interface. The calibration data can be found in the Appendix G. Instrument calibration data was used to convert the electrical signal into the actual pressure output – which is further used in facility process control.

3.4. Flow Measurement and Calibration

For the purpose of measuring flow, 3 types of flow meters were installed. The primary loop flow meter is a vortex shedding flow meter by Sierra instruments (Figure 3.6.). This flow meter operates on the von Karman effect, where a bluff body (Basically an obstruction in flow) creates vortices in the flow meters housing. The volume between two vortices is known based on the construction of the flow meter. The frequency of these vortices gives the flow rate in the loop. This flow meter also consists of a pressure sensor and an RTD to display local pressure and temperature, respectively.

Figure 3.6. Vortex shedding flow meter installed in the primary loop section.

Additionally, a Coriolis flow meter was also installed in the facility – which works on the Coriolis Effect giving the mass flow rate in the loop. For the subsequent experimentation, this flow meter was not used due to further calibrations and testing required for accurate experimentation. A turbine flow meter is utilized at the heat exchanger input to observe city water flow rate.

Calibration for the vortex shedding flow meter was performed by the manufacturer and the calibration data was applied to the LabVIEW program for accurate data conversion. Similar to the pressure transmitters, the signal received is in the range of 4 to 20 mA which was then scaled to the desired parameters. The calibration data for the vortex shedding flow meter can be viewed in Appendix G.

4. PROCESS CONTROL AND AUTOMATION

4.1. Control Valves

4.1.1. Temperature Control Valves

The CHF facility has its flow regulated using VFD connected pump. A continuous flow rate is sent via the city water lines. 2 pneumatically operated valves are present downstream, at the main flow line to the heat exchanger and the bypass line. These valves have SS-304 actuators operating using 80 to 100 psi compressed air. The valves were directly connected to the PLC system. The valve connected to the heat exchanger pipe can be observed in Figure 4.1.

Figure 4.1. Pneumatically operated temperature control valve which regulates flow through the heat exchanger.

Initially, the valves were inoperable due to outdated calibration and faulty connections. With the assistance of the TAMU Utilities personnel, these valves were

calibrated using an Emerson 475 Field Communicator device. For the smooth operation of these valves, connection and operation troubleshooting was initially performed, and compressed air lines were installed for their operation.

The temperature control valves operate in tandem with each other, For instance, if the downstream valve is x % open, the bypass valve is programmed to be (100 – x) % open. When the system heat is too large, the downstream valve opens, to allow the passage of cooling water to the heat exchanger, facilitating heat removal. Subsequently, for operation without power, all cooling water is bypassed due to no heal removal requirement.

4.1.2. Pressure Control Valves

Correspondingly, 2 pressure control valves are also present to adjust the N_2 input to the pressurizer and allow for the test section pressurization to prevent leaks. Valve connections and calibration were also performed. The same compressed air lines used for the temperature control valves were used, with extensions to the pressure control valves. These valves were also calibrated using the aforementioned valve field communicator device. In a similar operational design, pressurization of the system opens the primary pressure valve, to allow N_2 to inflate the pressurizer bladder. System depressurization is carried out using the exit valve, which releases N_2 from the bladder to the atmosphere. Two solenoid valves are present – one right after the N_2 tanks and one upstream from the valves, to isolate the N_2 tanks and the pressurizer respectively. Figure 4.2. shows the pressure control valves and N_2 tank grid.

Figure 4.2. Solenoid valves (in orange) along with the pneumatic pressure control valves. The grid is the high-pressure lines carrying compressed air to actuate the valves and N_2 tubing from the tanks, to pressurize the system.

4.2. PLC - DAQ - Ignition system

The control system (Figure 4.3.) will consist of a triangular network of the PLC, the DAQ and the system operating Ignition 7.9. A pair of low latency 75 inch touchscreen monitors have been extended from the desktop computers to operate the system using a touch interface. This network will retrieve data in real time, visually observe trends in system parameters and control all experimental variables.

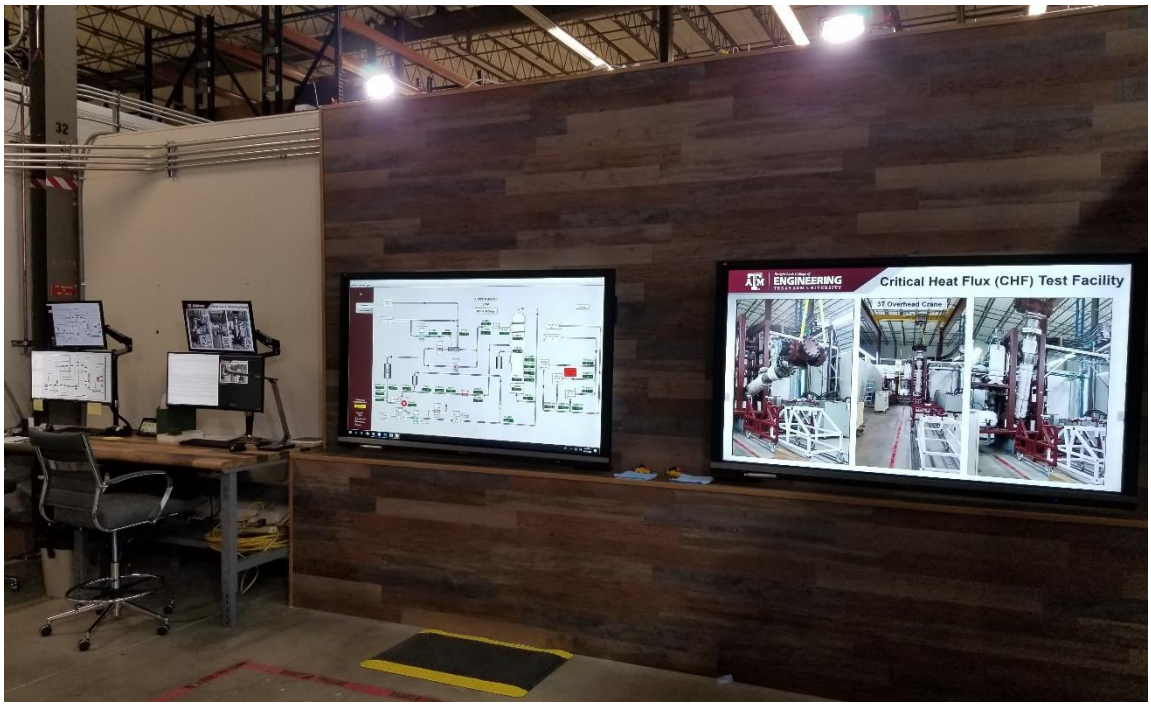

Figure 4.3. CHF facility control area consisting of desktops extended to touch panels.

4.2.1. Ignition 7.9

Ignition 7.9 – a process automation software – was used to remotely observe system parameters and save experiment data to a file for post processing. Ignition is a software platform for creating custom applications for process control [9]. It consists of a Human Machine Interface and SCADA. The interface was first studied and the project was customized according to the CHF Facility's requirements. The PLCs can be accessed via Ignition and connect to SQL databases. Ignition's high-performance historian was used to acquire data simultaneously with the LabVIEW data acquisition files. Ignition was used to monitor and control the data, manually or automatically based on test

conditions. Post installation, setting up and using a project was carried out using the following steps:

1. Launch the Gateway Webpage. The Gateway Webpage is where all of the information is stored, and where all of the general configuration was performed. Here, the device connections, database connections, security settings, backups were set up.
2. Launch the Designer. Once the connections were confirmed, the created project was accessed using Ignition's Designer Interface. Tags – to link PLC and LabVIEW data values to Ignition, query databases, show status, history trends, alarms, were configured using this Interface.
3. Save the project. When saved, Ignition sends all data and all changes back to the Gateway. Everything is centrally stored in the gateway allowing instantaneous project updates.

The Ignition interface is shown in Figure 4.4. Each process component is a configurable button that can be accessed via a mouse click or using touch interface via the touch panels. The set points can be manually adjusted to the desired values, causing Ignition to run the logic trees in the background. The pump set point, temperature control valve position, pressure control valve position are parameters that can manually be set to the required value. Correspondingly, all loop parameters and system variables can be monitored using the loop trends interface. This allows for an easy display of the variation in multiple parameters in once centralized interface.

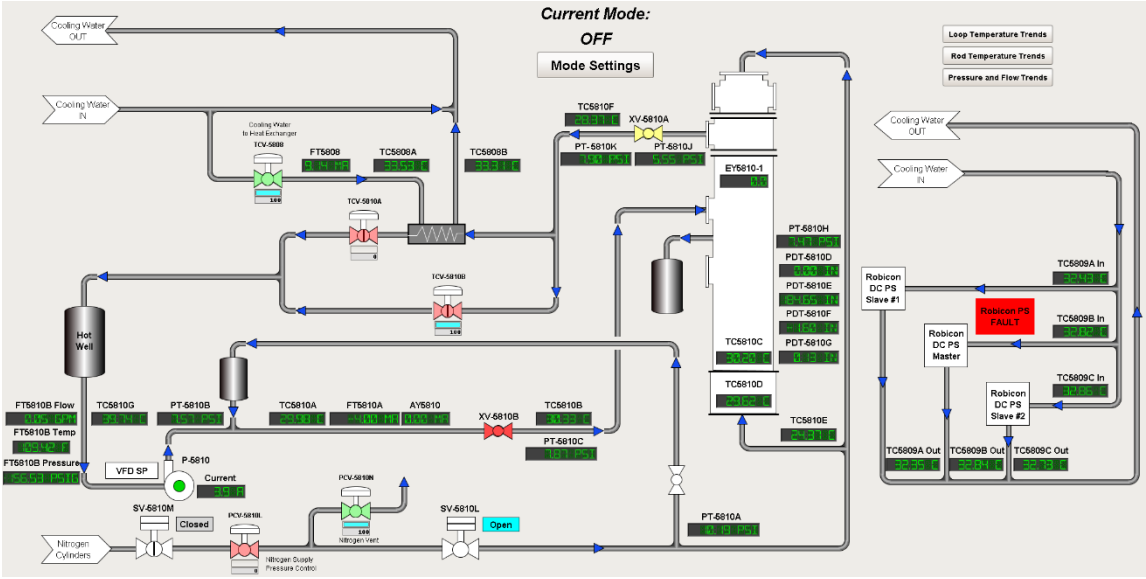

Figure 4.4. Ignition UI showing all updated components and real-time data.

4.2.2. LabVIEW and PLC-BedRock System

A LabVIEW program was created to host an OPC server, which when read by Ignition 7.9 updated the Ignition program to receive and interpret the process data. A PLC system was used for the automatic operation of all the control systems and devices. The PLC sends and assimilates the appropriate signals to the device of consideration and controls its behavior or response. This PLC was connected to a desktop computer with the NI DAQ and all the instrumentation. LabVIEW was used for data acquisition from the facility.

Simultaneously, the PLC system has its own OPC server – which sends process control related parameters to the desk computers which are remotely located. Ignition was programmed to control the valves, pump for flow, temperature and pressure control. Newer instrumentation was also added, mapped and tested using Ignition's graphical UI.

This included pump controls, valve controls as well as all pressure transmitter data, newer RTD and thermocouples. Tag paths were also linked to the PLC system, so that real time data can be used for process control. The control interface was redesigned for ease of use, and older parts that were not installed or which were unused were eliminated from the interface.

The LabVIEW OPC server was configured to read data from all pressure transmitters, flow meters, K-type thermocouples and RTDs. Figure 4.5. shows the OPC server program in the LabVIEW interface. The OPC server functions as a cloud which stores data and Ignition 7.9 was programmed to read this data and update the values to manipulate system parameters. The polling rated was set at 3 Hz, for real time data viewing calibrations were updated within the OPC server to display accurate readings in the units of choice.

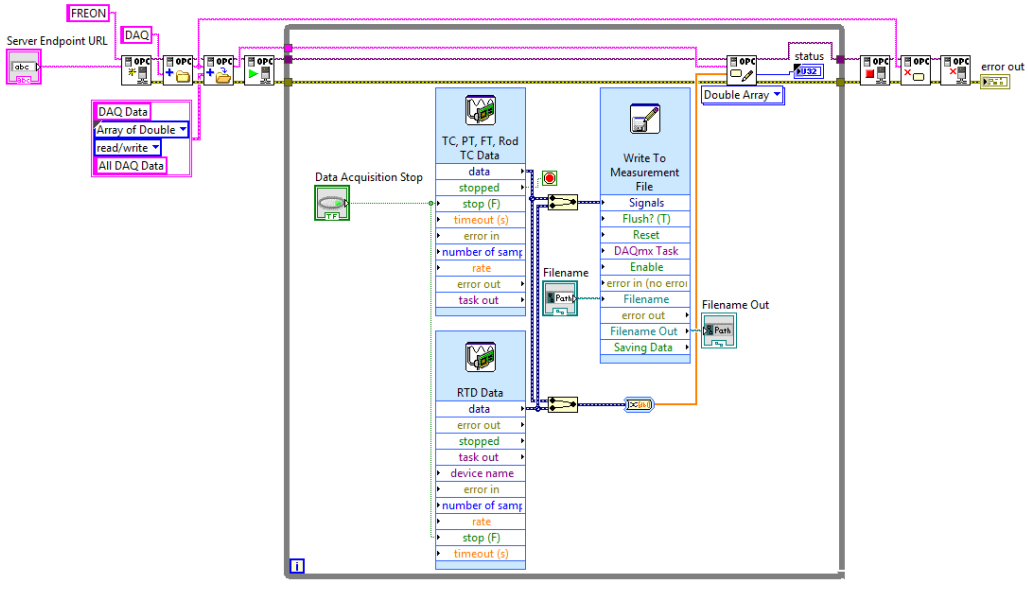

Figure 4.5. LabVIEW program which runs an OPC server to send and log data in real-time.

Data for post-processing was programmed to be acquired when the OPC server begins running. The logic by which the PLC operates was configured using BedRock IDE v1.8. Using this software, the logic diagrams previously used by Westinghouse Co. were first programmed. Based on the system upgrades and changes to the facility, the logic was updated as per requirement. The valves were reprogrammed for automation and the scale up multipliers were removed, which were used because the older nonoperational PLC was unable to decipher decimal places. These multiplier of 10 was added at various stages – which was subsequently removed from the logic since the new PLC is able to read decimal points. Systems communication was tested by first remotely opening & closing the valves independently. The pump was also tested by ramping up the VFD in 5% increments using Ignition; which the facility was filled with tap water. All the systems were tested and passed the individual working tests. Real time data viewing was also tested and the system updated the scaled valves to Ignition at the specified polling rate.

Ignition was also programmed to display real-time trends – which shows loop temperature trends. Similarly, flow rates for the 3 flow meters and pressure data from the 10 pressure transducers, as well as Rod thermocouple data from the 98 thermocouples was configured to be observed in real time.

5. EXPERIMENTAL

The following subsections describe the preparation for experimentation and the experimental methods followed. Since the facility is a complex amalgamation of many parts that are required to work synchronously with each other, it was necessary to ensure that all components were working in perfect order prior to any experimental test or component test.

5.1. Component Maintenance and Installations

Prior to the experimental procedure, a few important installations and maintenance tasks were performed, for the seamless operation of the CHF Facility which are explained in the following subsections.

5.1.1. Pressurizer servicing

The surge suppressor tank was not in operation of a long period of time, which led to rust formation on the inner walls. To remove the rust, the inner section was first scrubbed with a metal brush and larger flakes were vacuumed out. A rust removal solution was then used in batches to treat the finer rust present. The solution was allowed to treat the surface for 15 minutes, followed by removal with a cloth towel. This process was repeated several times till the fine coat of rust had been removed. Isopropyl alcohol was also used in the last phase, to clear any rust removal residue. A new bladder was purchased for future installation, but for the purpose of current tests, the previously used

bladder was employed. The pressurizer was then installed on the facility with the help of the overhead crane.

5.2. Preparation for Experimentation

Post the completion of all connections and maintenance, all connections – including pressure fittings for the pressure taps, valves and temperature sensor probe insertion pressure fittings – were checked. Prior to each experimental run or system test, the DAQ computer was switched on, followed by switching on the PLC system to allow these to initialize. The LabVIEW program was run on the desktop computer in the vicinity of the facility. Ignition 7.9 was run on the main workstation and it was confirmed each time whether all systems are communicating with each other. The OPC servers were tested for communication. If all systems and OPC servers were confirmed to be running, the test procedures could be initialized. If the pump was required to be used, the VFD was switched on. The compressed air line to the control valves was opened to allow air in the pressure range of 80 to 100 psi to actuate the valves.

5.3. Facility Fill

The CHF flow loop has to be ensured to be water solid – for accurate readings in pressure and flow rate. A specific procedure has been outlined to make sure that the facility has a continuous air free environment within the internals – based on prior experience. The facility fill procedure utilized for the purposes of this experimentation is described as follows:

1. A water hose was connected from the tap outlet to valve A located near TC5810 C (Figure 5.1.). Another water hose was connected from the outlet valve B near TC5810 G to a drain tank (Figure 5.2.).
2. The topmost outlet C – used for displacement for air and to ensure complete filling – was connected to a clear hose routed to the drain tank.
3. Valve A & C were opened completely, and valve B was shut.
4. The tap was opened completely, allowing water to fill the test section & air to escape from valve C.
5. When a constant flow was achieved from valve C, all pressure transducer liners in the pressure transducer grid were opened, one at a time, to purge any trapped air and to make the lines water solid. All valves for the pressure transducers were shut when it was ensured that they were purged.
6. Using Ignition, the pump was started in 5% increments to 20% (12 Hz) for 5 minutes, so that any air gaps or voids may be displaced.
7. Step 5 was repeated to remove these air gaps via the pressure transducer lines and valve C.
8. When the system seemed to be adequately degassed, the water input was stopped by first shutting down valve A and then turning off the city water input.
9. Repeat step 6 followed by opening valve C. If the stream was found to be constant – valve C was shut.
10. All valves were shut, to maintain a closed system.

Figure 5.1. Valve A connected to the test section which is used to fill the system.

Figure 5.2. Drain valve B near TC5810 G – which is the lowest accessible point in the system.

5.4. Facility Drain

Similar to filling facility with water, the facility has to be drained in a pre-outlined manner, to ensure that all the process fluid above the lowest point in the system (valve near TC5810 G) is drained. As mentioned below, compressed air at approximately 80 psig was used to drastically speed up this process. The CHF loop drain procedure is outlined below:

1. It was ensured that the pump was turned off and that all valves were closed before proceeding with system drainage.
2. The hose from valve A was attached to the drain tank.
3. Valves A, B & C were opened to release water from the system.
4. After a few minutes of drainage, the compressed air line was connected to the port near TC5810 F, to speed up facility water drain.
5. When valve A stopped releasing water, it was closed and the system allowed to drain from valve B.
6. Once completely drained, the compressed air line was shut off and then removed, and all open valves were completely closed.
7. The drain tank was then emptied appropriately, in a location safe for water drainage.

5.5. Facility Clean

Since the CHF loop was not in operation for a prolonged period of time, the facility was required to be adequately cleaned by forcing flow through the loop internals.

Sedimentation due to rust formation, particle accumulation and general system purging was targeted to be achieved by flowing water through the loop for a time interval in the range of 10 to 15 minutes per cycle.

1. The facility was first filled using the ‘Facility Fill’ procedure.
2. After ensuring complete facility fill, the pump was run at 20% for 5 minutes and at 50% for another 5 minutes.
3. The facility was the drained – based on the ‘Facility Drain’ procedure to remove settled impurities.
4. Steps 2 & 3 were repeated twice more to obtain clear water.

5.6. System Pressurization Tests

To test the pressure control valves and the ability of the CHF loop to hold pressure, it was decided to undertake pressurization tests using the combination of the process control software, N_2 for pressurization and the pressure control valves. The tests were of an observatory nature, to understand a few important factors. Firstly, it was required to know whether the pressure control valves were operating appropriately, even at high pressures – adequately controlling the system pressure. Secondly, it was essential to confirm that the control system pressurizes the loop and equally essential to ascertain whether it depressurizes from the high pressures it attains. Debugging and troubleshooting was further carried out post completion of these tests. The procedure by which these tests were carried out is explained as stated:

1. The facility was filled completely using the facility fill procedure.
2. The N_2 lines were connected to the pressurizer and the N_2 tanks were then opened.
3. Compressed air was then supplied to all the valves to facilitate their actuation.
4. The set point on Ignition – for PCV5810 L – was first set at 10 psig.
5. Solenoid valve SV5810 M was first opened, then SV5810 L was opened – allowing N_2 to fill the pressurizer.
6. Once the desired pressure was attained, it was allowed to hold pressure to observe if there was any pressure loss.
7. SV5810 M was left opened and the set point for pressure valve PCV5810 N was then set at a lower value, initially 0 psig.
8. It was then checked to see if the system depressurizes appropriately.
9. This was further repeated for various system pressures – in 50 psig increments from 0 to 200 psig.
10. Following completion of the pressurization tests, the system was safely depressurized to atmospheric pressure.

5.7. Isothermal Pressure Drop Tests

Following system pressurization tests, isothermal pressure drop tests were conducted. The aim of these tests was to first test for system automation and complete operation using the Ignition 7.9 interface. The target of these tests was to ensure successful pressurization to the desired pressure set-point, to carry out forced flow

within the system and to acquire data remotely as well as locally, with the software employed in the test loop.

5.7.1. Test Conditions

The test was initiated at atmospheric pressure and static process fluid, here water. It should be noted that the valve PCV5810 N has an offset of 3 psig, to avoid unnecessary depressurization of the system. Data was logged using both LabVIEW and Ignition at a sample frequency of 17 Hz and a sample rate of 17 per sample log. The ambient temperature of the surroundings was approximately 22°C.

The uncertainty in the vortex flow meter was 0.7% of the reading, as obtained from the calibration documents. The pressure transmitters possess an uncertainty of 0.1% of their measurements. The measurement uncertainties were propagated based on the uncertainties in density and dynamic viscosity.

5.7.2. Test Procedure

The procedure followed is for the isothermal tests is described below.

1. The facility was filled completely using the facility fill procedure.
2. The N_2 lines were connected to the pressurizer and the N_2 tanks were then opened.
3. Compressed air was then supplied to all the valves to facilitate their actuation.
4. The set point on Ignition – for PCV5810 N – was first set at -3 psig.
5. Solenoid valve SV5810 L was opened – allowing system depressurization.

6. The pump was switched on using the VFD switch on Ignition. The set point was ramped up to 10% of 60 Hz.
7. The flow rate was allowed to stabilize at each ramp rate for a period of 20 s. Data was acquired for 10 s after a stable flow rate was achieved.
8. The pump set point was increased in 10 % increments for VFD drive rates of 20% to 70%. Step 7 was followed at each set point.
9. The pump set point was then decreased in 10 % increments from 70% to 10% while following step 7 at each set point.
10. The system was then pressurized for loop pressures of 50, 100, 150 and 250 psig. Steps 6 to 9 were repeated at each loop pressure. If the loop had a lower pressure than required, SV5810 M was manually opened using the override command, to pressurize the system further.
11. After data acquisition and test completion, the loop was safely depressurized to atmospheric pressure and the VFD was shut down.

6. RESULTS AND DISCUSSION

6.1. System Clean

As stated in the previous section, the system was cleaned using a combination of facility fill, operating the facility to regulate flow and draining the system thrice. Figure 6.1. shows the progression of process fluid quality within the system. As observed in the figure, the initial run resulted in the removal of larger particles and loose rust. The possible locations from which the rust originates was concluded to be from the pressurizer, the parts within the hot well or un-serviced rod bundle. Figure 6.2. shows the quality of water as the procedure was repeated for the second time. It should be noted that the residue in the second run is that of sedimentation accumulating below the valve at TC5810 G, which is the lowest point in the system.

Figure 6.1. First run facility drain water with suspended rust from facility internals.

Figure 6.2. Second facility cleaning run which yielded remaining rust particles and cleaning product.

Figure 6.3. Final cleaning run resulting in clear water indicating clean internals.

The final cleaning run resulted in considerable clear water (Figure 6.3.). The residue on the walls of the drain tank causes the color of the water to be slightly brown – whereas the water was found to be clear. After satisfactory results in cleaning the facility, the facility was filled with clean water to commence with the system pressurization tests.

6.2. System Pressurization Tests

The system pressurization tests were performed to observe whether the system could be operated automatically using Ignition. Figure 6.4. shows the variation of system pressure in Pa as the test was commenced. The labels in Figure 6.4. are described in Table 6.1.

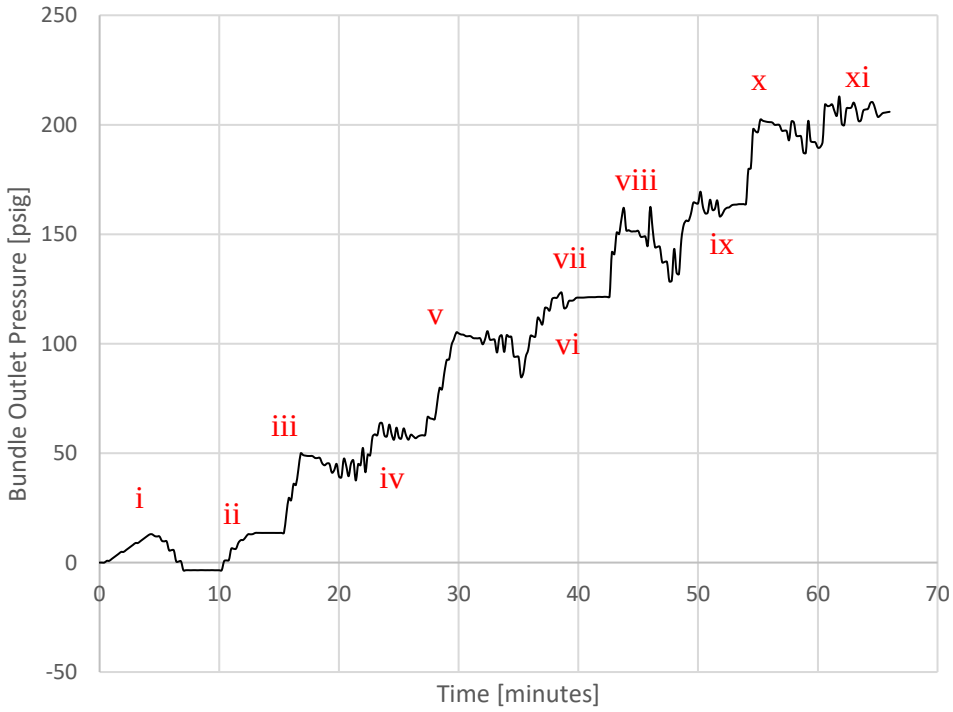

Figure 6.4. System pressurization test results at static flow.

Table 6.1. System pressurization test label description.

Label	Process
i	Test initiation.
ii	Pressure ramp up to 10 psig and stabilization.
iii	Pressure ramp up to 50 psig and stabilization.
iv	Valve response to stabilize system pressure to set point.
v	Pressure ramp up to 100 psig and stabilization.
vi	Excess valve depressurization as compensation.
vii	Pressure ramp up to 125 psig and stabilization.
viii	Pressure ramp up to 150 psig.
ix	Excess depressurization and overcompensation.
x	Pressure ramp up to 200 psig.
xi	Valve open/shut to compensate for set point stabilization.

Initially the system was pressurized to 10 psig to test if the N_2 system was functional using the control system. When it was observed to maintain the pressure set point, it was then increased in small increments. The set points were arbitrarily selected to be: 50, 100, 125, 150, 160 and 200 psig.

The figure shows that pressure ramps go slightly above the set point, as observed with any standard control system. The phase around 10 minutes into the tests displays a negative pressure due to the pressure transducer at the outlet relaying back pressure data before stabilizing to display actual pressure. The pressure was ramped up again to 10 psig to check for stability – which it was observed to attain.

On increasing the set point to 50 psig, the same principle of over pressurizing the system was followed, as programmed in the logic system that controls the PLC. The

spikes and drops show the system trying to attain the set point by controlling the pressure control valves. In this case, the solenoid control valves were manually operated to control the N_2 input due to a limited amount of N_2 being available for test purposes. It should also be noted that the spikes and drops seems more pronounced due to the data collected being in the scale of 12 seconds per point to avoid data collection value overflow – which resulted in the LabVIEW program to terminate.

The valve PCV5810 N, which is the N_2 release valve, was programmed to open only for a pressure difference of 3 psig above the set point, to account for the response time of the pressure control valve. These are high proportional and differential gain valves – used for instant shutoff or open of the valves.

The pressure valves for set points 100, 150 and 200 psig show this response and its behavior in real time. Larger drops are observed due to the system being unable to respond fast enough to the difference of actual pressure and the set point. This can be remedied by increasing the difference of set point and the actual pressure to a valve of 5 psig or greater to reduce the amount of N_2 being removed from the system and to maintain the system pressure.

On increasing the pressure to 150 psig and 200 psig, this effect is slightly more pronounced and exaggerated due to the constant pressurization and depressurization of the system. Following completion of this test, the system was depressurized to atmospheric pressure for safety purposes.

6.3. Isothermal Pressure Drop Tests

The experimentation was conducted using aforementioned tests conditions. A variation in temperature was observed due to the work output by the magnetically coupled pump. The actual data acquired for pressure was in inches H_2O for the differential pressure transducers and in psig for the gauge pressure transducer. These converted into Pascal for uniformity. Similarly, the original data acquired by the flow meter in gallons/ min was converted to m^3/s.

Each data value for Temperature, Flow Rate and differential pressure was averaged from the data set which the LabVIEW program acquired. These consisted of 289 samples per second, for the duration of the test period. Microsoft Excel was used to post-process this data for further analysis. Since the temperature displayed a variation, the fluid properties – here, fluid density and dynamic viscosity – was estimated at each temperature using the NIST webbook water property data. The Kinematic viscosity (m^2/s) was further calculated using the following expression:

$$\nu = \frac{\mu}{\rho}$$

It should also be noted that the area of flow in the test section is dissimilar to the cross sectional area for the flow meter. The fluid velocity (m/s) for the bundle cross section area – available for flow – was calculated using the given expression:

$$v = \frac{Q}{A_{CS}}$$

Subsequently the Reynolds number was calculated using the alternate form of the classical expression.

$$Re = \frac{\rho . v . D_H}{\mu} = \frac{Q . D_H}{\nu . A_{CS}}$$

The geometrical parameters of the test section is seen in the Table 6.2. The flow area was calculated by subtracting the area occupied by each heated rod from the total available cross-sectional area of the test section. The hydraulic diameter (m) – a property used to describe the effective flow diameter was calculate using the expression:

$$D_H = \frac{4A}{P}$$

Table 6.2. Important geometrical parameters for the CHF test section.

Geometric Parameter	Notation	Parameter Value
Hydraulic Diameter	D_H	0.0098 m
Flow Cross Section Area	A_{CS}	0.0024 m^2
Rod Bundle Length	L_{Rod}	0.254 m
Length between consecutive spacer grids	L	0.03175 m

6.3.1. Pressure Drop for n =1 and n = 6

Tables 6.3. to 6.7. summarize the experimental test results for the thermal hydraulic parameters (T, p, Q, v, Re) and the fluid properties estimated at the respective operating average temperatures. The pump was controlled using the VFD – which was increased in 5% increments – to increase the volumetric flow within the facility. The tables display the results for each operating pressure, beginning at atmospheric pressure and culminating at 200 psig, in 50 psig increments by supplying N_2 to the pressurizer.

Table 6.3. Thermal hydraulic parameter data for 0 psig system pressure.

VFD (%)	Frequency (Hz)	T (°C)	Q (m^3/s)	dp (n=1) (Pa)	dp (n=6) (Pa)	ρ (kg/m^3)	μ (Pa.s)	ν (m^2/s)	Re (-)	v (m/s)
10	6	21.408	0.0020	329.957	3400.967	997.92	9.680E-04	9.700E-07	8424.34	0.834
20	12	21.498	0.0033	1195.286	12331.919	997.90	9.680E-04	9.700E-07	14019.40	1.388
30	18	21.526	0.0051	2634.272	26889.221	997.89	9.680E-04	9.700E-07	21651.94	2.143
40	24	21.587	0.0068	4569.641	46781.406	997.88	9.680E-04	9.700E-07	28533.78	2.824
50	30	21.670	0.0086	7029.365	70776.518	997.86	9.680E-04	9.700E-07	36313.70	3.594
60	36	21.899	0.0106	9623.214	101997.798	997.81	9.680E-04	9.701E-07	44621.46	4.417
70	42	22.110	0.0122	13837.410	134526.294	997.76	9.680E-04	9.701E-07	51534.55	5.102

Table 6.4. Thermal hydraulic parameter data for 50 psig system pressure.

VFD (%)	Frequency (Hz)	T (°C)	Q (m^3/s)	dp (n=1) (Pa)	dp (n=6) (Pa)	ρ (kg/m^3)	μ (Pa.s)	ν (m^2/s)	Re (-)	v (m/s)
10	6	22.417	0.0016	329.262	3506.527	997.84	9.449E-04	9.469E-07	6919.54	0.669
20	12	22.422	0.0033	1214.808	12606.332	997.84	9.449E-04	9.469E-07	14324.46	1.384
30	18	22.438	0.0051	2658.521	27348.473	997.83	9.449E-04	9.469E-07	21988.70	2.125
40	24	22.473	0.0068	4636.429	47321.425	997.83	9.449E-04	9.469E-07	29165.91	2.818
50	30	22.585	0.0086	7134.170	72643.771	997.80	9.449E-04	9.469E-07	37066.01	3.582
60	36	22.778	0.0103	10203.707	101795.516	997.76	9.449E-04	9.470E-07	44616.69	4.311
70	42	22.985	0.0121	13784.901	138077.433	997.71	9.449E-04	9.470E-07	52326.15	5.057

Table 6.5. Thermal hydraulic parameter data for 100 psig system pressure.

VFD (%)	Frequency (Hz)	T (°C)	Q (m^3/s)	dp (n=1) (Pa)	dp (n=6) (Pa)	ρ (kg/m^3)	μ (Pa.s)	ν (m^2/s)	Re (-)	v (m/s)
10	6	23.273	0.0016	325.583	3465.750	997.81	9.261E-04	9.281E-07	7093.45	0.672
20	12	23.267	0.0033	1223.591	12463.775	997.81	9.261E-04	9.281E-07	14648.38	1.387
30	18	23.279	0.0051	2629.936	26927.209	997.81	9.259E-04	9.279E-07	22247.94	2.106
40	24	23.319	0.0068	4604.556	46596.598	997.80	9.250E-04	9.270E-07	30067.85	2.844
50	30	23.433	0.0086	7103.249	71476.017	997.77	9.226E-04	9.247E-07	38051.80	3.590
60	36	23.563	0.0103	10176.805	101619.163	997.74	9.199E-04	9.219E-07	45520.61	4.282
70	42	23.783	0.0121	13659.788	136767.547	997.69	9.152E-04	9.173E-07	53744.62	5.031

Table 6.6. Thermal hydraulic parameter data for 150 psig system pressure.

VFD (%)	Frequency (Hz)	T (°C)	Q (m^3/s)	dp (n=1) (Pa)	dp (n=6) (Pa)	ρ (kg/m^3)	μ (Pa.s)	ν (m^2/s)	Re (-)	v (m/s)
10	6	22.417	0.0016	327.081	3511.342	998.15	9.446E-04	9.464E-07	6694.61	0.646
20	12	22.422	0.0036	1209.614	12411.897	998.15	9.446E-04	9.464E-07	15371.50	1.484
30	18	22.438	0.0051	2624.936	26854.756	998.15	9.442E-04	9.459E-07	22064.44	2.130
40	24	22.473	0.0070	4555.421	46333.699	998.14	9.435E-04	9.453E-07	30226.72	2.916
50	30	22.585	0.0086	7019.568	70704.861	998.11	9.409E-04	9.426E-07	37175.09	3.576
60	36	22.778	0.0105	9961.163	100416.448	998.07	9.367E-04	9.385E-07	45618.63	4.369
70	42	22.985	0.0121	13480.426	135253.871	998.02	9.321E-04	9.339E-07	52851.67	5.037

Table 6.7. Thermal hydraulic parameter data for 200 psig system pressure.

VFD (%)	Frequency (Hz)	T (°C)	Q (m^3/s)	dp (n=1) (Pa)	dp (n=6) (Pa)	ρ (kg/m^3)	μ (Pa.s)	ν (m^2/s)	Re (-)	v (m/s)
10	6	24.758	0.0015	314.633	3496.905	997.73	8.946E-04	8.967E-07	7052.80	0.645
20	12	24.731	0.0037	1188.643	12259.310	997.74	8.953E-04	8.973E-07	17018.59	1.558
30	18	24.737	0.0051	2602.306	26635.346	997.74	8.950E-04	8.971E-07	23063.89	2.111
40	24	24.767	0.0068	4529.518	46021.838	997.73	8.944E-04	8.965E-07	31093.94	2.844
50	30	24.835	0.0086	6985.091	70474.706	997.71	8.930E-04	8.951E-07	39377.00	3.596
60	36	24.967	0.0105	9925.558	99621.164	997.68	8.904E-04	8.924E-07	48240.04	4.393
70	42	25.326	0.0123	13379.297	134509.941	997.59	8.831E-04	8.853E-07	56519.71	5.106

Figure 6.5. displays the pressure drop per characteristic length for n = 1 spacer grid. Additionally, from the expression for differential pressure, it was confirmed that the pressure drop across the rod bundle was independent of the operating pressure. This can be observed by the similarity and proximity of the curves – at the average operating pressure. The minimum and maximum Re were 5863.2 and 56519.7, respectively – which were well into the turbulent regime (Re > 2000). The pressure drop depends solely upon the Reynolds number, as seen from the expressions for the friction factor and grid loss coefficient. The uncertainties in differential pressure were included in the figure but are too small to decipher. This is due to the high accuracy of the pressure sensors – which possess an uncertainty of 0.1% of the measurement.

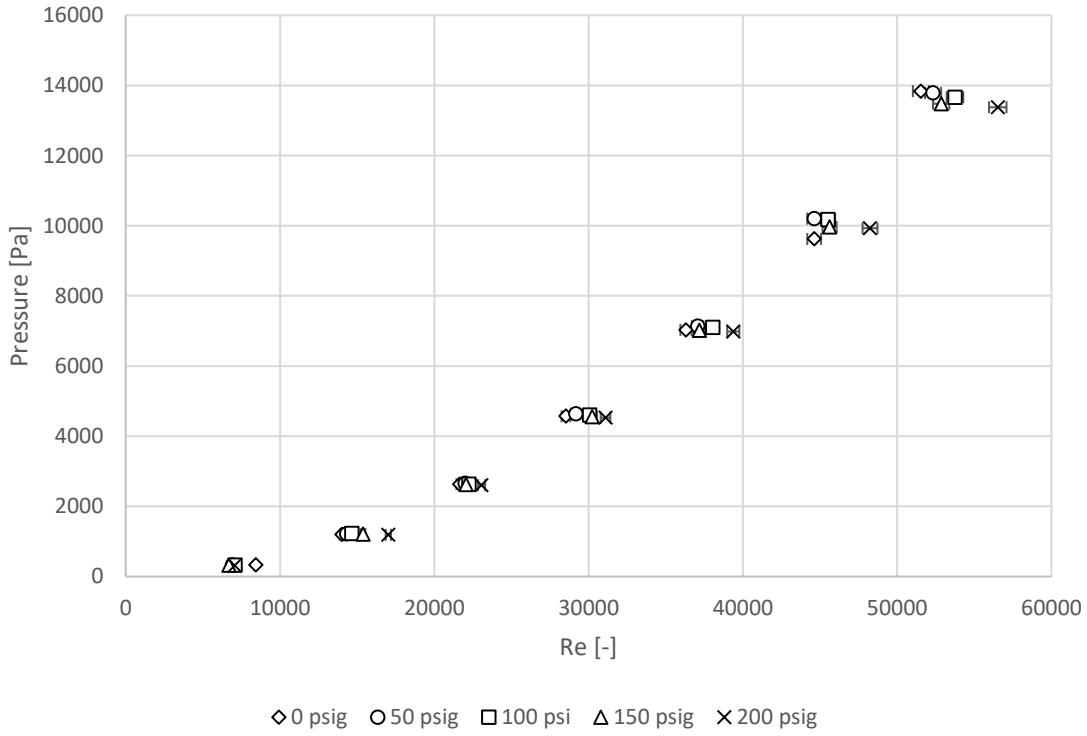

Figure 6.5. Pressure drop for n = 1 spacer grid with respect to Re for 50 psig increments in system pressure.

Figure 6.6. shows the variation of differential pressure for increments in Re – for n = 6 spacer grids. Similar to the results obtained for n =1, the differential pressure for 6 spacer grids and the characteristic flow length was also found to display a similar shape, with a higher span of pressure. The uncertainties have also been added in the figure.

Analogous to Figure 6.5., the pressure sensor uncertainties are very small to notice. The uncertainty in Re is also observed, but is small enough because of the high precision of the vortex shedding flow meter. Re uncertainty is small enough, noticeable only at higher volumetric flow rates. This confirms the accuracy of the measurement sensors and their accuracy – which will be used for future experiments.

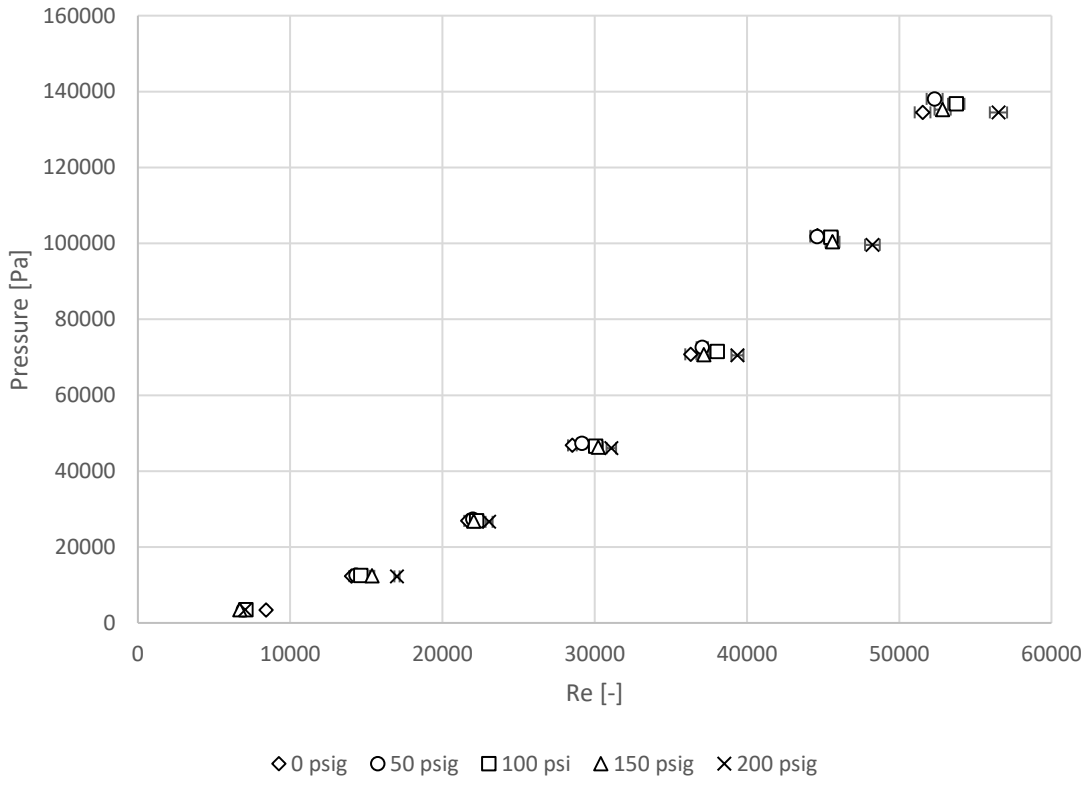

Figure 6.6. Pressure drop variation with Re for n = 6 spacer grids with 50 psig increments in system pressure.

6.3.2. Friction Factor and Spacer Grid Loss Coefficients

Subsequently, to obtain the friction factor, the Blasius Correlation for smooth pipes was used [3]. It is given as follows.

$$f = 0.316\ Re^{-0.25}$$

This expressions disregards any effects of the spacer grids causing a disturbance in the local Reynolds number. Alternatively, for comparison, the correlation for the friction factor of the Rod Bundle which was employed in the Cobra-TF computational code was used, which is as follows [10]:

$$f = 0.204\ Re^{-0.2}$$

The parameter 'L' was for the characteristic length of rods with the spacer grids which was encompassed by the differential pressure transducer in use. For 6 spacer grids (n =6), the length was estimated to be 0.1905 m. Similarly, for just one spacer grid, L was estimated to be 0.03175 m. Following the estimation of friction factor, the grid loss coefficient was back calculated from the pressure drop (Pa) expression, given below. The values for the friction factor for 6 spacer grids was calculated using the Blasius and CTF correlations [2] [11].

$$\Delta p = \left(\frac{f.L}{D_H} + n.K_{SG}\right).\frac{1}{2}\rho v^2$$

$$\therefore\ K_{SG} = \frac{1}{n}\left(\frac{2\Delta p}{\rho v^2} - \frac{f.L}{D_H}\right)$$

These values were compared to the KAERI friction factor correlations for a similarly shaped spacer grid. The correlations were only for 1 and 3 spacer grids and are mentioned as follows [11] [12]:

$$K_{SG-1} = 4.3269\ Re^{-0.1269}$$

$$K_{SG-3} = 4.7393\ Re^{-0.1288}$$

Table 6.8. to 6.12. shows the estimated friction factors and the spacer grid loss coefficient. The values for n = 1 are observed to be sufficiently similar to the KAERI correlations. A noted difference in the values is observed to exist due to the use of regular city water with impurities as well as the difference in the shape of the spacer grids used in each case. Correspondingly, the values of K for n = 6 was observed to be of a similar locus as obtained from the correlations.

Table 6.8. Calculated friction factors and spacer grid loss coefficients for 0 psig system pressure.

VFD (%)	Frequency (Hz)	Re (-)	$f_{Blasius}$ (-)	f_{CTF} (-)	$K_{Blasius}$ (n=1)	K_{CTF} (n=1)	$K_{Blasius}$ (n=6)	K_{CTF} (n=6)	K_{SG-1} (n=1)	K_{SG-3} (n=3)
10	6	8424.34	0.0330	0.0335	0.8443	0.8428	1.5271	1.5256	1.3741	1.4795
20	12	14019.40	0.0290	0.0302	1.1501	1.1463	2.0453	2.0415	1.2881	1.3855
30	18	21651.94	0.0261	0.0277	1.0651	1.0598	1.8713	1.8659	1.2190	1.3101
40	24	28533.78	0.0243	0.0262	1.0694	1.0633	1.8803	1.8742	1.1770	1.2643
50	30	36313.70	0.0229	0.0250	1.0163	1.0096	1.7558	1.7490	1.1416	1.2257
60	36	44621.46	0.0217	0.0240	0.9182	0.9110	1.6761	1.6689	1.1121	1.1936
70	42	51534.55	0.0210	0.0233	0.9978	0.9903	1.6589	1.6514	1.0920	1.1716

Table 6.9. Calculated friction factors and spacer grid loss coefficients for 50 psig system pressure.

VFD (%)	Frequency (Hz)	Re (-)	$f_{Blasius}$ (-)	f_{CTF} (-)	$K_{Blasius}$ (n=1)	K_{CTF} (n=1)	$K_{Blasius}$ (n=6)	K_{CTF} (n=6)	K_{SG-1} (n=1)	K_{SG-3} (n=3)
10	6	6919.54	0.0346	0.0348	1.3642	1.3636	2.5083	2.5078	1.4089	1.5174
20	12	14324.46	0.0289	0.0301	1.1775	1.1736	2.1048	2.1009	1.2846	1.3817
30	18	21988.70	0.0259	0.0276	1.0964	1.0910	1.9399	1.9345	1.2166	1.3075
40	24	29165.91	0.0242	0.0261	1.0918	1.0856	1.9122	1.9060	1.1738	1.2608
50	30	37066.01	0.0228	0.0249	1.0410	1.0342	1.8181	1.8113	1.1386	1.2224
60	36	44616.69	0.0217	0.0240	1.0299	1.0227	1.7592	1.7520	1.1121	1.1936
70	42	52326.15	0.0209	0.0232	1.0131	1.0055	1.7366	1.7290	1.0899	1.1693

Table 6.10. Calculated friction factors and spacer grid loss coefficients for 100 psig system pressure.

VFD (%)	Frequency (Hz)	Re (-)	$f_{Blasius}$ (-)	f_{CTF} (-)	$K_{Blasius}$ (n=1)	K_{CTF} (n=1)	$K_{Blasius}$ (n=6)	K_{CTF} (n=6)	K_{SG-1} (n=1)	K_{SG-3} (n=3)
10	6	7093.45	0.0344	0.0346	1.3345	1.3338	2.4539	2.4533	1.4044	1.5126
20	12	14648.38	0.0287	0.0300	1.1813	1.1773	2.0704	2.0664	1.2810	1.3777
30	18	22247.94	0.0259	0.0276	1.1041	1.0987	1.9434	1.9379	1.2148	1.3055
40	24	30067.85	0.0240	0.0259	1.0631	1.0568	1.8464	1.8401	1.1692	1.2558
50	30	38051.80	0.0226	0.0247	1.0312	1.0243	1.7790	1.7721	1.1348	1.2183
60	36	45520.61	0.0216	0.0239	1.0423	1.0350	1.7812	1.7739	1.1093	1.1905
70	42	53744.62	0.0208	0.0231	1.0148	1.0072	1.7384	1.7308	1.0862	1.1653

Table 6.11. Calculated friction factors and spacer grid loss coefficients for 150 psig system pressure.

VFD (%)	Frequency (Hz)	Re (-)	$f_{Blasius}$ (-)	f_{CTF} (-)	$K_{Blasius}$ (n=1)	K_{CTF} (n=1)	$K_{Blasius}$ (n=6)	K_{CTF} (n=6)	K_{SG-1} (n=1)	K_{SG-3} (n=3)
10	6	6694.61	0.0349	0.0350	1.4549	1.4545	2.6924	2.6921	1.4148	1.5239
20	12	15371.50	0.0284	0.0297	1.0080	1.0038	1.7891	1.7850	1.2732	1.3692
30	18	22064.44	0.0259	0.0276	1.0756	1.0702	1.8932	1.8878	1.2161	1.3069
40	24	30226.72	0.0240	0.0259	0.9961	0.9898	1.7426	1.7363	1.1685	1.2550
50	30	37175.09	0.0228	0.0249	1.0264	1.0195	1.7730	1.7662	1.1382	1.2220
60	36	45618.63	0.0216	0.0239	0.9759	0.9686	1.6873	1.6800	1.1090	1.1902
70	42	52851.67	0.0208	0.0232	0.9974	0.9898	1.7133	1.7057	1.0885	1.1678

Table 6.12. Calculated friction factors and spacer grid loss coefficients for 200 psig system pressure.

VFD (%)	Frequency (Hz)	Re (-)	$f_{Blasius}$ (-)	f_{CTF} (-)	$K_{Blasius}$ (n=1)	K_{CTF} (n=1)	$K_{Blasius}$ (n=6)	K_{CTF} (n=6)	K_{SG-1} (n=1)	K_{SG-3} (n=3)
10	6	7052.80	0.0345	0.0347	1.4029	1.4022	2.6938	2.6932	1.4055	1.5137
20	12	17018.59	0.0277	0.0291	0.8917	0.8871	1.5972	1.5927	1.2568	1.3514
30	18	23063.89	0.0256	0.0274	1.0873	1.0817	1.9134	1.9078	1.2093	1.2995
40	24	31093.94	0.0238	0.0258	1.0452	1.0388	1.8234	1.8170	1.1643	1.2504
50	30	39377.00	0.0224	0.0246	1.0099	1.0029	1.7477	1.7408	1.1299	1.2130
60	36	48240.04	0.0213	0.0236	0.9620	0.9546	1.6556	1.6483	1.1012	1.1817
70	42	56519.71	0.0205	0.0229	0.9626	0.9549	1.6578	1.6501	1.0793	1.1578

Figures 6.7. to 6.11. display the calculated friction factors with respect to Reynolds number, as the volumetric flow rate was increased, for each system operating pressure. As previously discussed in the estimation of Pressure drops, the friction factors within the rod bundle rely solely on the Reynolds number. That is why there is a stark similarity in the shape and the experimentally calculated values for each operating pressure from 0 to 200 psig in 50 psig increments.

The Blasius friction factor was estimated to be slightly higher, which is due to the fact that the Blasius friction factor considers a single circular tube which is perfectly smooth. Hence the values overshoot that of the actual friction factor. Consequently, since the Cobra TF friction factor accounts for the rod roughness and geometry in fully developed flow, the values were found to be lower than the Blasius friction factor.

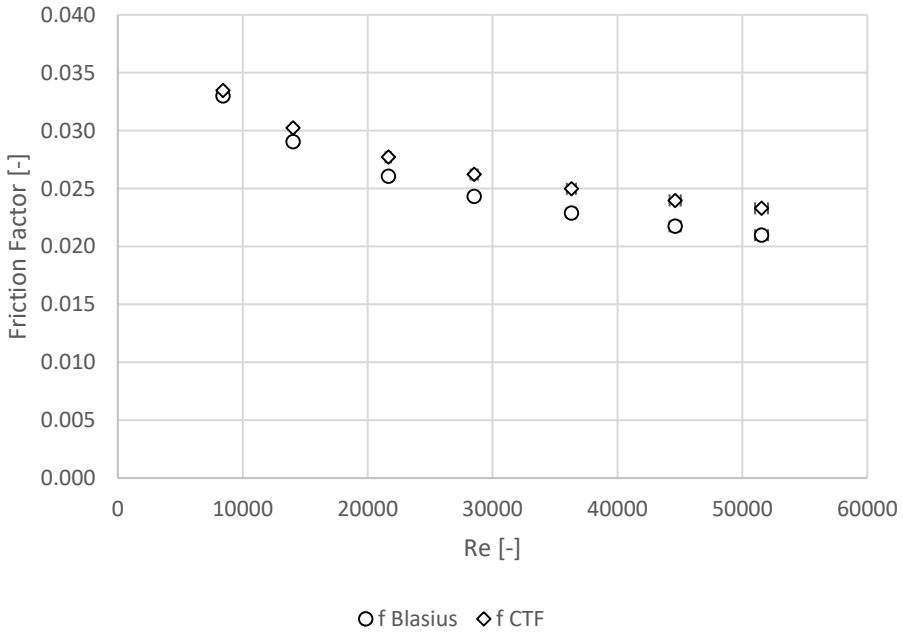

Figure 6.7. Blasius and Cobra TF friction factors for increasing Re at 0 psig.

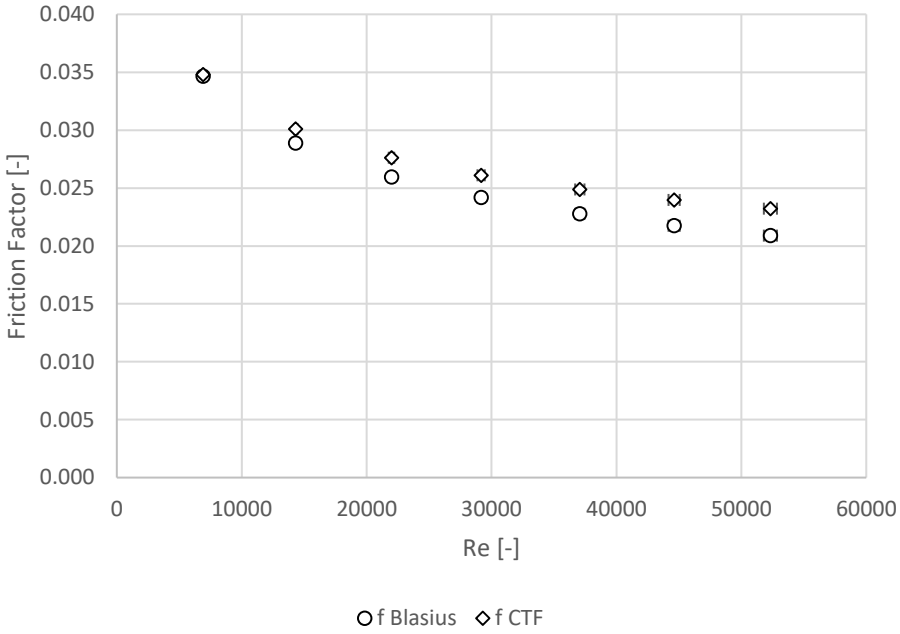

Figure 6.8. Blasius and Cobra TF friction factors for increasing Re at 50 psig.

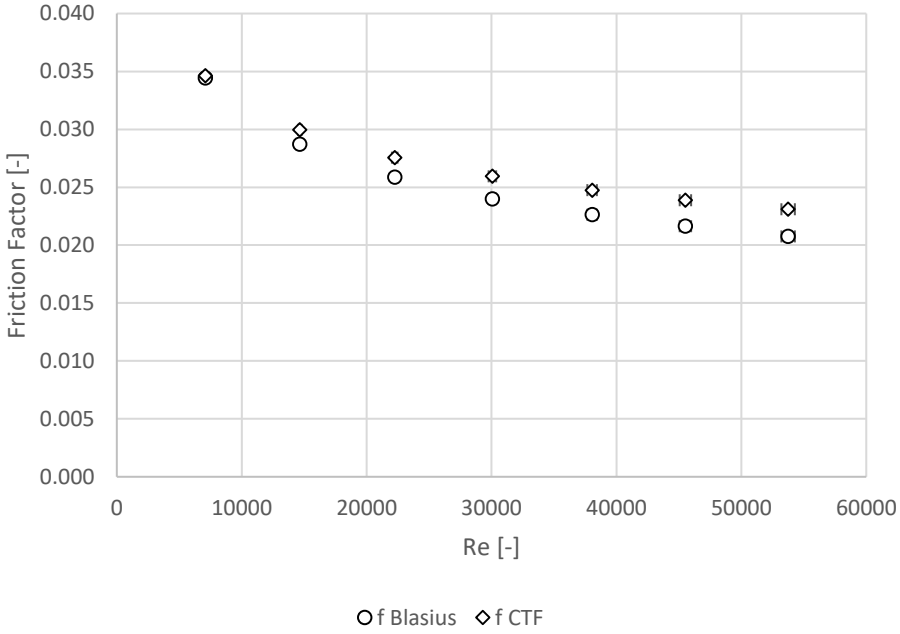

Figure 6.9. Blasius and Cobra TF friction factors for increasing Re at 100 psig.

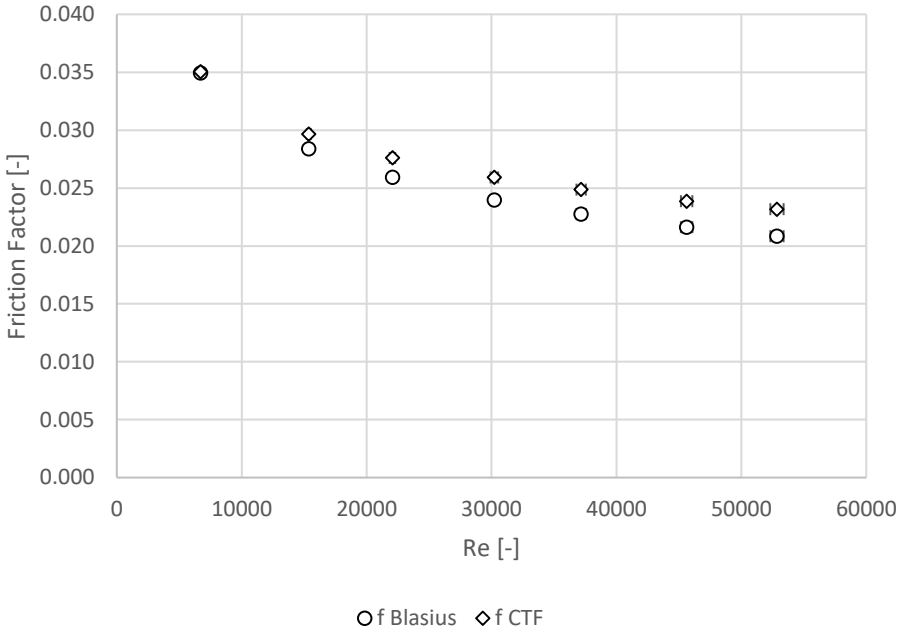

Figure 6.10. Blasius and Cobra TF friction factors for increasing Re at 150 psig.

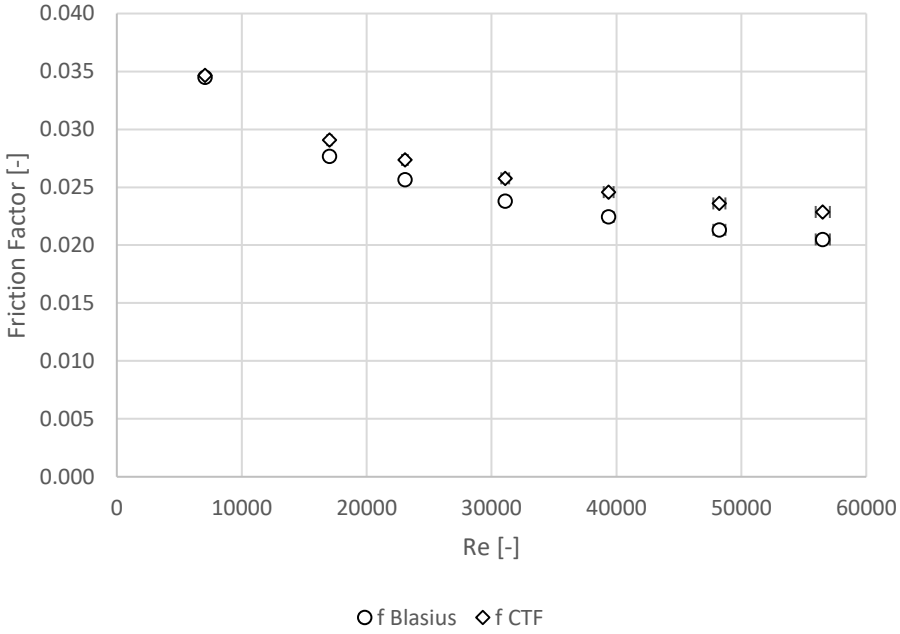

Figure 6.11. Blasius and Cobra TF friction factors for increasing Re at 200 psig.

The estimated spacer grid loss coefficients versus Re, for 50 psig increments in system pressure – from 0 to 200 psig – are seen in Figures 6.12. to 6.16. For a single spacer grid and one characteristic length between two consecutive spacer grids, the values using both friction factors were found to be very close to the KAERI spacer grid correlations obtained in literature. A high similarity of spacer grid coefficients was obtained, between the Blasius and Cobra TF friction factors, due to the higher dependence of spacer grid loss coefficients on the differential pressure rather than the friction factor. The KAERI grid loss coefficients for 3 spacer grids was found to be higher than all grid loss coefficients for 1 spacer grid – which was expected due to higher frictional losses. Similarly, for n = 6, the estimated values were found to be significantly greater, again due to higher losses in pressure, as the number of spacer grids are increased in the rod bundle.

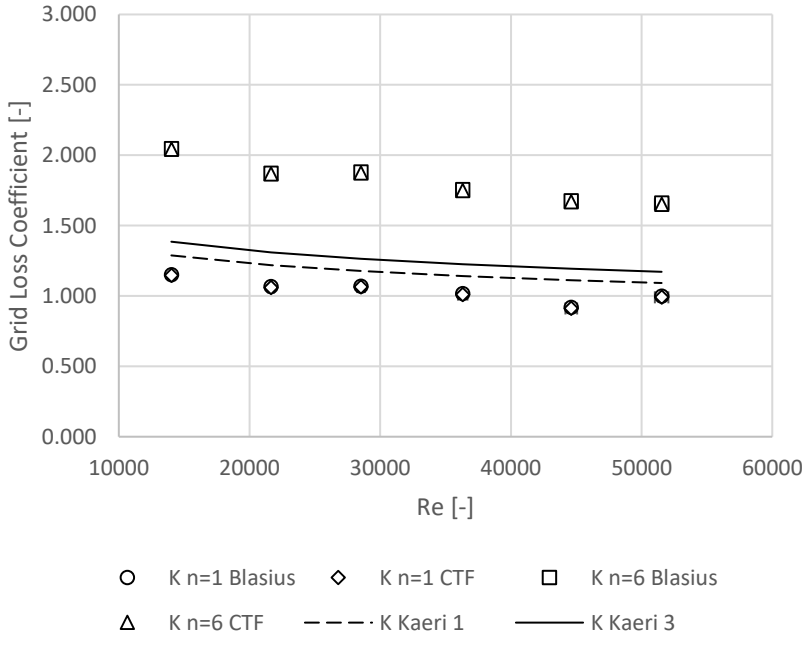

Figure 6.12. Variation of grid loss coefficients for increasing Re at 0 psig.

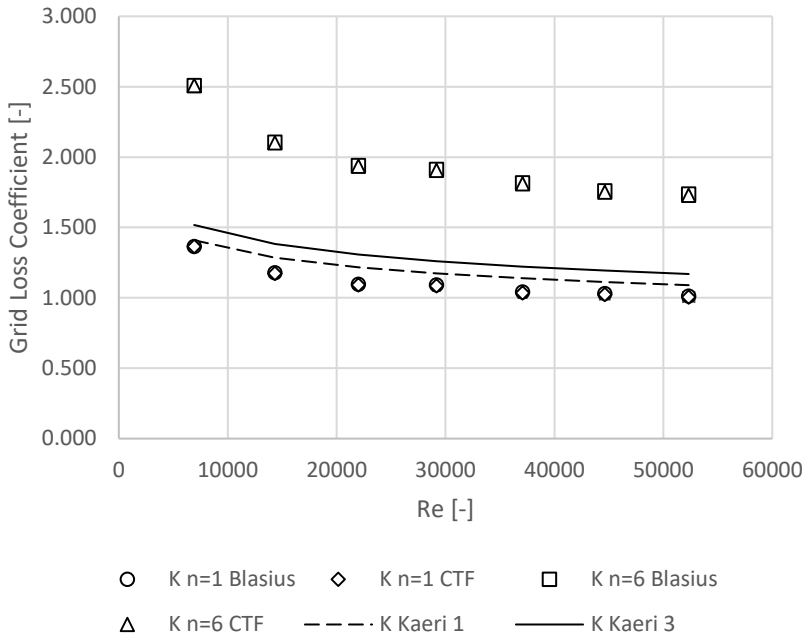

Figure 6.13. Variation of grid loss coefficients for increasing Re at 50 psig.

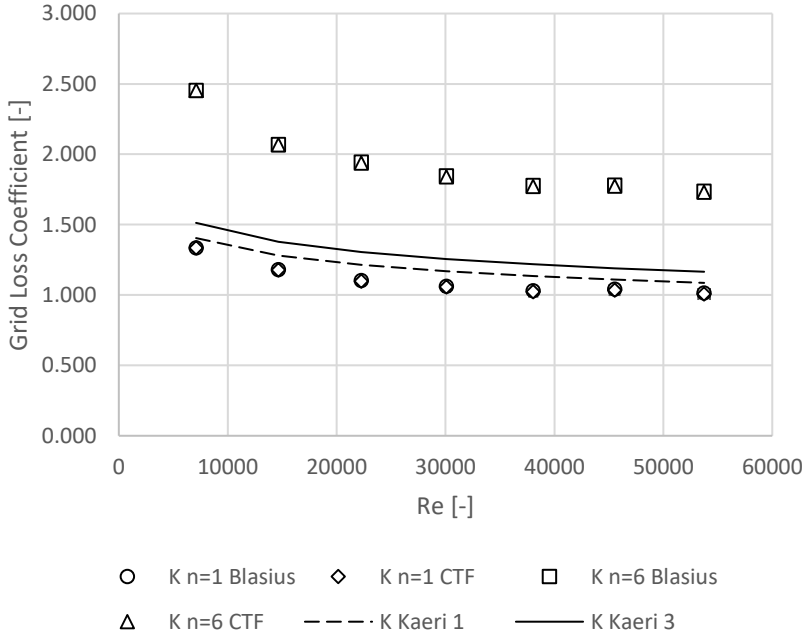

Figure 6.14. Variation of grid loss coefficients for increasing Re at 100 psig.

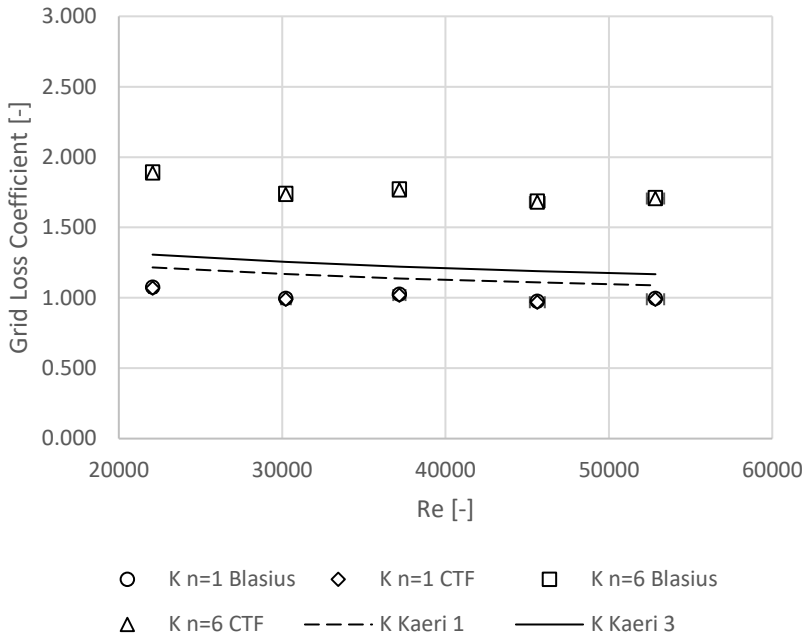

Figure 6.15. Variation of grid loss coefficients for increasing Re at 150 psig.

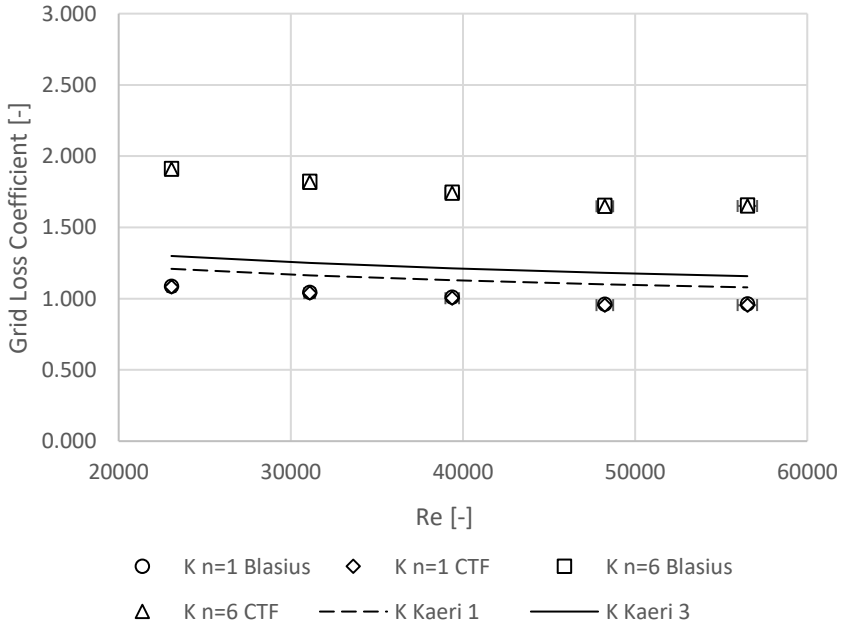

Figure 6.16. Variation of grid loss coefficients for increasing Re at 200 psig.

The uncertainty was propagated for the experimental measurements and can be observed in all of the figures. The uncertainties in Re arose from the dynamic viscosity, density and flow rate uncertainties. This is observable in the graphical plots. The uncertainties in Re become more pronounced at higher Re values, due to a greater uncertainty of measurement by the vortex shedding flow meter. Since the 2σ method was used to determine uncertainty, 95% of all obtained values should be included in the uncertainty bars. Subsequently, for the friction factor & space grid loss coefficient, the uncertainty was due to its dependence on Re. The uncertainties in friction factor and spacer grid loss coefficients were too insignificant to notice in the graphical plots. This can be attributed to the measurement accuracy of the pressure transducers and the negative power dependence of the uncertainty on Re. The propagated data for all uncertainties can be obtained in Appendix H.

7. CONCLUSIONS

7.1. Summary

The TAMU Critical Heat Flux Test Facility was upgraded considerably since its acquisition. These upgrades included reinstallation of instrumentation to acquire temperature, pressure and flow parameter data. The thermal hydraulic parameter sensors were calibrated to ensure their accuracy and dependability for measurement in sensitive and extreme conditions.

The experimental capabilities of the CHF Facility was further enhanced by incorporating system process control and remote operation. This was performed with a view of operating the facility under safe conditions, without having to be in close proximity during experimental tests. Further, the possibility of conducting simultaneous computational simulations is also allowed since the facility can be operated remotely. This can be performed to observe experimental data in real-time while simultaneously comparing it to the data obtained for computational method. In the process of engineering the facility's automation, the components were required to be debugged – to account for logic flow changes in the operation of process control components such as valves and the pump. This system troubleshooting also allowed for improvement in response times and fine tuning the process control of the facility.

To test the automation capabilities, the pressure tests were successfully carried out. The only inherent drawback was the system response time – due to the limitations in the gain of the process control valves. Prior to the tests, the facility was adequately

cleaned and serviced to ensure that the experimental results were as close as possible to pure water. The maximum possible impurities were removed from the system by a series of system fill, forced flow and system drain, with water.

The experimental tests carried out with water to confirm the system's operation displayed results consistent with literature. The pressure drop for a characteristics rod bundle length between two spacers and once spacer grid was experimentally obtained. This was performed for increments in Reynolds number at 50 psig increments in system pressure from approximately 0 psig to 200 psig. Similarly, the pressure drop variation with respect to Re was also experimentally estimated – for 6 characteristic rods lengths and 6 spacer grids. Both results displayed consistency in the general shape. It was also seen that the pressure drops are independent of system pressure and only display a direct dependence on Reynolds No.

The friction factors for the rod length were estimated. The Blasius friction factor and the CHF friction factor were estimated and compared graphically. These displayed a very high similarly in calculated values which was probably due to the similarities of local conditions and the proximity of constants within their respective correlations.

The grid loss coefficients – an estimate of energy loss due to turbulence and friction induced in the spacer grids – were calculated. For n = 1, the values were in close proximity to KAERI correlations for 1 and 3 spacer grids obtained from literature. The possible deviation from the exact values of the correlation can be attributed to the difference in geometry of the spacer grids used as well as the difference in conditions of

experimentation. All uncertainties were propagated to observe the dependability on these experimental results.

The facility upgrades and experimentation were concluded to be successful. Thermal hydraulic tests were viable to be carried out remotely with full operation and under extreme experimental conditions, involving high temperatures, pressures and Reynolds Number – within the mechanical limitations for the CHF facility. Future experiments are also ready to be conducted on the facility by changing the experimental parameters.

7.2. Future Scope

The subsequent project phase would primarily focus on the remote operation of the CHF facility with automated process control employing the use of DC power heating. Actual CHF tests can be conducted after the DC power tests are confirmed to be functional. Tests confirming the heat rejection via the heat exchanger are essential to be carried out. Subsequently, the refrigerant R-11 will be used as the process fluid. R-11 is a scaling fluid which possesses a low boiling point and a high vapor pressure – allowing experimental observations at two phase conditions and near accident conditions without the use of high power and very high pressurization levels. Computer simulations can also be verified with actual experimentation for pressure drop and CHF testing. [13]

Following the preliminary experimentation, to fully utilize the capability of the CHF facility, it is imperative to utilize the latest high fidelity instrumentation and measuring techniques. As an example, optical fibers can be used to detect the axial

temperatures of the fuel rod bundle. Optical fibers can also detect local void fractions within the rod bundle.

New fuel assemblies for Generation 3+ and Generation 4 designs of Nuclear Reactors operating using pressurized light water can be experimented on in the CHF Facility. This can be achieved by simply modifying the rod bundle and designing an adequate electrical conduction mechanism for the newer fuel rod designs to be studied. Similarly, if the need arises to study and develop new spacer grid designs, thermal hydraulic experimentation can be conducted using the TAMU CHF Facility.

REFERENCES

[1] Y. A. Cengel, "Introduction to Thermodynamics and Heat Transfer, 2nd Edition," McGraw-Hill Higher Education, 2009, pp. 515-532.

[2] N. E. Todreas and M. S. Kazimi, "Nuclear Systems I - Thermal Hydraulic Fundamentals," Taylor & Francis Group, 1990, pp. 382-397.

[3] H. Blasius, The Law of Similarity for Fricitional Processes in Fluids, Berlin, 1913.

[4] L. D. Smith III, P. F. Joffre, J.-M. Le Corre, F. Waldemarsson, A. Hallehn and H. Tejne, "High Resolution Thermal Mixing at Westinghouse ODEN Loop," in *NURETH-16*, Chicago, U.S.A., 2015.

[5] J.-M. Le Corre, U. C. Bergmann, A. Hallehn, H. Tejne, F. Waldemarsson, B. Morenius and R. Baghai, "Detailed Measurements of Local Parameters in Annular Two-Phase Flow in Fuel Bundle Under BWR Operating Conditions," in *NURETH-16*, Chicago, U.S.A., 2015.

[6] O. Wieckhorst, J. Kronenberg, H. Gabriel, S. Opel, D. Kreuter, T. Berger, R. Harne, K. Greene and F. Filhol, "AREVA's Test Facility KATHY: Robust Critical Heat Flux Measurements, A Prerequisite for Reliable CHF Prediction," in *Proceedings of the 2014 22nd International Conference on Nuclear Engineering - ICONE 22*, Prague, Czech Republic, 2014.

[7] M. Corradini and M. S. Greenwood, "Critical Heat Flux Phenomena at High Pressure & Low Mass Fluxes: NEUP Final Report Part I: Experiments," NEUP, 2014.

[8] A. Salahudidin, J. A. Khan, L. D. I. Smith and C. Wilbur, "Critical Heat Flux (CHF) and cold-flow pressure drop investigations of R-11 in a vertical iniformly heated 5x5 rod bundle.," *ASME Summer Heat Transfer Conference,* vol. 4, pp. 1-3, 2005.

[9] Inductive Automation, "Ignition 7.9 User Manual," 2015.

[10] R. K. Salko, T. S. Blyth, C. A. Dances, J. W. Magedanz, C. Jernigan, J. Kelly, A. Toptan, M. Gergar, C. Gosdin, M. N. Avramora, S. Palmtag and J. C. Gehin, "CTF Validation and Verification," U.S. Department of Energy, 2016.

[11] S. K. Yang and M. K. Chung, "Turbulent Flow Through Spacer Grids in Rod Bundles," *Transactions of the ASME,* vol. 120, p. 788, 1998.

[12] T.-H. Chun and D.-S. Oh, "A Pressure Drop Model for Spacer Grids with and without Flow Mixing Vanes," *Journal of Nuclear Science and Technology,* pp. 508-510, 1998.

[13] X. Cheng and U. Muller, "Review on Critical Heat Flux in Water Cooled Reactors," *Forschungszentrum Karlsruhe GmbH, Karlsruhe,* pp. 5-7, 2003.

APPENDIX A – PRESSURE TRANSDUCER INFORMATION AND CONNECTIONS

Order on Shroud Box	Label No.	Make	Serial No.	Location	Wire Polarity	Ethernet Wire Color Code	Connection in the DAQ Card 7
1	PDT5810 D	Rosemount Pressure Transmitters - Emerson Electric Co.	0778854	DP 12	Positive	Solid Blue	VSUP 1
					Negative	Blue/White	AI 1
2	PT5810 A		0778870	N2	Positive	Solid Orange	VSUP 2
					Negative	Orange/White	AI 2
3	PT5810 B		0778849	Pump	Positive	Solid Green	VSUP 3
					Negative	Green/White	AI 3
4	PDT5810 E		0778855	DP 23	Positive	Solid Brown	VSUP 4
					Negative	Brown/White	AI 4
5	PT5810 H		0778851	Bundle Exit 1	Positive	Solid Blue	VSUP 8
					Negative	Blue/White	AI 8
6	PDT5810 G		1324430	DP 13	Positive	Solid Orange	VSUP 9
					Negative	Orange/White	AI 9
7	PDT5810 F		0778856	DP 34	Positive	Solid Green	VSUP 10
					Negative	Green/White	AI 10
8	PT5810 K		0778853	Bundle Exit 2	Positive	Solid Brown	VSUP 11
					Negative	Brown/White	AI 11
9	PT5810 C		0778853	Inlet	Positive	Solid Blue	VSUP 12
					Negative	Blue/White	AI 12
10	PT5810 J		0778850	Outlet	Positive	Solid Orange	VSUP 13
					Negative	Orange/White	AI 13

APPENDIX B – FLOW METER INFORMATION AND CONNECTIONS

Component	Label	Location	Make	Model No.	Serial No.	Wire Color	Wire Polarity (Connection on Unit)	Connection in the DAQ Card 7
Coriolis Flow Meter	FT5810 A Power	Pump Upstream	Micro Motion Inc.	DS30031563U	2157048 (191632)	Red	+ VDC In (17)	AI 14
						Black	Power Return (18)	AI SENSE
Vortex Shedding Flow Meter	FY5810 B Signal	Pump Downstream	Sierra Instruments Inc.	2401-VTP-1-G7-E2-DD-P2-V6H-ST-MP4	11986	Brown	4-20 mA Pressure Out (7)	AI 16
						Brown/White	Ground (8)	AI SENSE
						Blue	4-20 mA Temperature Out (9)	AI 17
						Blue/White	Ground (10)	AI SENSE
						Orange	4-20 mA Flow Rate Out (11)	AI 18
						Orange/White	Ground (12)	AI SENSE
Turbine Flow Meter	FT5808	Heat Exchanger Flow Out	Rosemount Vortex 8800	CF020SA1N1D1M5	50105	Red	Positive	VSUP
						Black	Negative	AI23

APPENDIX C – THERMOCOUPLE INFORMATION AND CONNECTIONS

DAQ Card No.	Label No.	Make	Serial No.	Location	Connection in the DAQ Card
4	TE5810A	Omega Engineering Inc.	KMQXL-125G-6	Pump Upstream	TC 21
	TE5810D		KQXL-125G-3.5	Test Section Bottom	TC 22
	TE5810E		KQXL-125G-3.5	Low Melt Heater	TC 23
	TE5810F		KMQXL-125G-6	Test Section Outlet	TC 24
	TE5810G		KQXL-125G-3.5	Pump Downstream	TC 25
	TE5809A In		KMQXL-125G-6	Robicon Slave #1 Water Supply Inlet	TC 26
	TE5809A Out		KMQXL-125G-6	Robicon Slave #1 Water Supply Outlet	TC 27
	TE5809B In		KMQXL-125G-6	Robicon Master Water Supply Inlet	TC 28
	TE5809B Out		KMQXL-125G-6	Robicon Master Water Supply Outlet	TC 29
	TE5809C In		KMQXL-125G-6	Robicon Slave #2 Water Supply Inlet	TC 30
	TE5809C Out		KMQXL-125G-6	Robicon Slave #2 Water Supply Outlet	TC 31

APPENDIX D – RTD INFORMATION AND CONNECTIONS

Card No.	Label No.	Make	Serial No.	Location	Wire Color Code	Wire Polarity	Channel	Connection in the DAQ Card
9	TE5810B	Omega Engineering Inc.	P-M-1/10-1/8-6-0-G-3 DTC-U-M DTC-U-F	Test Section Inlet	Red	Positive	CH 0	EX +
					Black	Negative		EX -
					White	Positive		AI +
					Green	Negative		AI -
	TE5810C		P-M-1/10-1/8-6-0-G-3 DTC-U-M DTC-U-F	Test Section Bottom	Red	Positive	CH 1	EX +
					Black	Negative		EX -
					White	Positive		AI +
					Green	Negative		AI -
	TE5808A		P-M-1/10-1/8-6-0-G-3 DTC-U-M DTC-U-F	Heat Exchanger Outlet	Red	Positive	CH 2	EX +
					Black	Negative		EX -
					White	Positive		AI +
					Green	Negative		AI -
	TE5808B		P-M-1/10-1/8-6-0-G-3 DTC-U-M DTC-U-F	Heat Exchanger Inlet	Red	Positive	CH 3	EX +
					Black	Negative		EX -
					White	Positive		AI +
					Green	Negative		AI -

APPENDIX E – ROD THERMOCOUPLE CONNECTIONS

Card No.	Sr. No.	Group	Series	Connection in the DAQ Card
1	1	J 01	01-11	TC 0
	2		01-21	TC 1
	3		02-11	TC 2
	4		02-12	TC 3
	5		02-21	TC 4
	6		02-22	TC 5
	7		03-11	TC 6
	8		03-12	TC 7
	9		03-21	TC 8
	10		03-22	TC 9
	11		04-11	TC 10
	12		04-12	TC 11
	13		04-21	TC 12
	14		04-22	TC 13
	15		05-11	TC 14
	16		05-12	TC 15
	17		05-21	TC 16
	18		05-22	TC 17
	19	J 02	06-11	TC 18
	20		06-12	TC 19
	21		06-21	TC 20
	22		06-22	TC 21
	23		07-11	TC 22
	24		07-12	TC 23
	25		07-21	TC 24
	26		07-22	TC 25

Card No.	Sr. No.	Group	Series	Connection in the DAQ Card
2	1	J 03	08-11	TC 0
	2		08-12	TC 1
	3		08-21	TC 2
	4		08-22	TC 3
	5		09-11	TC 4
	6		09-12	TC 5
	7		09-21	TC 6
	8		09-22	TC 7
	9		10-11	TC 8
	10		10-22	TC 9
	11		10-12	TC 10
	12		10-21	TC 11
	13		11-11	TC 12
	14		11-12	TC 13
	15		11-21	TC 14
	16		11-22	TC 15
	17		12-11	TC 16
	18		12-12	TC 17
	19		12-21	TC 18
	20		12-22	TC 19
	21	J 04	13-11	TC 20
	22		13-12	TC 21
	23		13-21	TC 22
	24		13-22	TC 23
	25		14-11	TC 24
	26		14-12	TC 25
	27		14-21	TC 26
	28		14-22	TC 27

Card No.	Sr. No.	Group	Series	Connection in the DAQ Card
3	1	J 05	15-11	TC 0
	2		15-12	TC 1
	3		15-21	TC 2
	4		15-22	TC 3
	5		16-11	TC 4
	6		16-12	TC 5
	7		16-21	TC 6
	8		16-22	TC 7
	9		17-11	TC 8
	10		17-21	TC 9
	11		18-11	TC 10
	12		18-21	TC 11
	13		19-11	TC 12
	14		19-21	TC 13
	15	J 06	20-11	TC 14
	16		20-21	TC 15
	17		21-11	TC 16
	18		21-21	TC 17
	19		22-11	TC 18
	20		22-21	TC 19
	21		23-11	TC 20
	22		23-21	TC 21
	23		24-11	TC 22
	24		24-21	TC 23
	25		25-11	TC 24
	26		25-21	TC 25

Card No.	Sr. No.	Group	Series	Connection in the DAQ Card
4	1	J 07	17-12	TC 0
	2		17-22	TC 1
	3		18-12	TC 2
	4		18-22	TC 3
	5		19-12	TC 4
	6		19-22	TC 5
	7		20-12	TC 6
	8		20-22	TC 7
	9		21-12	TC 8
	10		21-22	TC 9
	11		22-12	TC 10
	12		22-22	TC 11
	13		23-12	TC 12
	14		23-22	TC 13
	15		24-12	TC 14
	16		24-22	TC 15
	17		25-12	TC 16
	18		25-22	TC 17

APPENDIX F – TEMPERATURE SENSOR CALIBRATION DATA

Group	Sensor	Type	Time (s)	Set Point (°C)	Average Temperature (°C)	
					Reference Probe	Loop Probe
1	TE5810 C	RTD	300	-	0.000	-0.030
				20	21.776	21.720
				150	124.898	125.769
				250	211.734	212.578
				-	250.000	251.201
	TE5810 D	TC	300	-	0.000	-1.148
				20	21.776	21.439
				150	124.898	135.883
				250	211.734	226.380
				-	250.000	268.889
	TE5810 E	TC	300	-	0.000	-1.717
				20	21.776	21.382
				150	124.898	134.988
				250	211.734	227.380
				-	250.000	269.551

Group	Sensor	Type	Time (s)	Set Point (°C)	Average Temperature (°C)	
					Reference Probe	Loop Probe
2	TE5809 A In	TC	300	-	0.000	0.023
				20	22.860	23.111
				150	131.742	135.918
				250	215.300	220.300
				-	250.000	256.355
	TE5809 A Out	TC	300	-	0.000	0.015
				20	22.860	23.141
				150	131.742	136.119
				250	215.300	220.643
				-	250.000	256.741

Group	Sensor	Type	Time (s)	Set Point (°C)	Average Temperature (°C)	
					Reference Probe	Loop Probe
3	TE5809 B In	TC	300	-	0.000	-0.350
				20	22.860	23.001
				150	122.569	122.852
				250	224.792	226.847
				-	250.000	252.022
	TE5809 B Out	TC	300	-	0.000	-0.282
				20	22.860	22.987
				150	122.569	122.896
				250	224.792	226.611
				-	250.000	251.811
	TE5809 C In	TC	300	-	0.000	-0.316
				20	22.860	22.987
				150	122.569	123.142
				250	224.792	227.035
				-	250.000	252.311
	TE5809 C Out	TC	300	-	0.000	-0.403
				20	22.860	22.999
				150	122.569	123.217
				250	224.792	227.470
				-	250.000	252.762

Group	Sensor	Type	Time (s)	Set Point (°C)	Average Temperature (°C)	
					Reference Probe	Loop Probe
4	TE5808 A	RTD	300	-	0.000	-0.327
				20	21.465	21.489
				150	128.094	124.562
				250	211.956	207.137
				-	250.000	243.242
	TE5810 A	TC	300	-	0.000	-0.962
				20	21.465	21.759
				150	128.094	128.447
				250	211.956	216.844
				-	250.000	254.871
	TE5810 G	TC	300	-	0.000	-0.123
				20	21.465	21.858
				150	128.094	131.657
				250	211.956	217.561
				-	250.000	256.735

Group	Sensor	Type	Time (s)	Set Point (°C)	Average Temperature (°C)	
					Reference Probe	Loop Probe
5	TE5810 B	RTD	300	-	0.000	-0.609
				20	22.644	22.639
				150	128.621	130.453
				250	215.574	219.675
				-	250.000	254.675
	TE5808 B	RTD	300	-	0.000	0.383
				20	21.759	21.983
				150	133.002	129.773
				250	225.306	221.122
				-	250.000	244.906
	TE5810 F	TC	300	-	0.000	0.420
				20	21.759	22.013
				150	133.002	135.484
				250	225.306	227.367
				-	250.000	252.742

APPENDIX G – PRESSURE SENSORS AND FLOW METER CALIBRATION DATA

Sensor	Slope (m)	y-intercept (c)
PT5810 A	37495.8299	-149.9737
PT5810 B	37492.8380	-149.8923
PT5810 C	37503.3819	-150.0345
PT5810 H	37506.1160	-150.0394
PDT5810 D	9377.2733	-37.52847
PDT5810 E	15621.18925	-62.46854
PDT5810 F	15621.03108	-62.48234
PDT5810 G	46876.89003	-187.40153
PT5810 J	37486.8627	-149.8465
PT5810 K	37508.5158	-149.9865
FT5810 B	15623.0470	-62.4770

APPENDIX H – UNCERTAINTY PROPAGATION DATA

Uncertainty Data for 0 psig system pressure:

VFD (%)	Freq. (Hz)	σ_Q (m^3/s)	σ_v (m^2/s)	σ_{Re} (-)	$\sigma_{f\text{-}Blasius}$ (-)	$\sigma_{f\text{-}CTF}$ (-)	$\sigma_{K\text{-}Blasius}$ (n=1)	$\sigma_{K\text{-}CTF}$ (n=1)	$\sigma_{K\text{-}Blasius}$ (n=6)	$\sigma_{K\text{-}CTF}$ (n=6)	$\sigma_{K\text{-}SG\text{-}1}$ (n=1)	$\sigma_{K\text{-}SG\text{-}3}$ (n=3)
10	6	1.40E-06	9.70E-09	84.45	8.27E-05	6.71E-05	1.33E-03	1.33E-03	2.29E-03	2.29E-03	1.75E-03	1.88E-03
20	12	2.33E-06	9.70E-09	140.54	7.28E-05	6.06E-05	1.74E-03	1.74E-03	3.00E-03	3.00E-03	1.64E-03	1.76E-03
30	18	3.60E-06	9.70E-09	217.05	6.53E-05	5.55E-05	1.61E-03	1.61E-03	2.74E-03	2.74E-03	1.55E-03	1.67E-03
40	24	4.74E-06	9.70E-09	286.04	6.09E-05	5.26E-05	1.61E-03	1.61E-03	2.74E-03	2.74E-03	1.50E-03	1.61E-03
50	30	6.04E-06	9.70E-09	364.03	5.74E-05	5.01E-05	1.53E-03	1.53E-03	2.56E-03	2.56E-03	1.45E-03	1.56E-03
60	36	7.42E-06	9.70E-09	447.31	5.45E-05	4.81E-05	1.38E-03	1.38E-03	2.45E-03	2.45E-03	1.41E-03	1.52E-03
70	42	8.57E-06	9.70E-09	516.61	5.26E-05	4.67E-05	1.49E-03	1.49E-03	2.42E-03	2.42E-03	1.39E-03	1.49E-03

Uncertainty Data for 50 psig system pressure:

VFD (%)	Freq. (Hz)	σ_Q (m^3/s)	σ_v (m^2/s)	σ_{Re} (-)	$\sigma_{f\text{-}Blasius}$ (-)	$\sigma_{f\text{-}CTF}$ (-)	$\sigma_{K\text{-}Blasius}$ (n=1)	$\sigma_{K\text{-}CTF}$ (n=1)	$\sigma_{K\text{-}Blasius}$ (n=6)	$\sigma_{K\text{-}CTF}$ (n=6)	$\sigma_{K\text{-}SG\text{-}1}$ (n=1)	$\sigma_{K\text{-}SG\text{-}3}$ (n=3)
10	6	1.12E-06	9.47E-09	69.36	8.68E-05	6.98E-05	2.07E-03	2.07E-03	3.67E-03	3.67E-03	1.79E-03	1.93E-03
20	12	2.33E-06	9.47E-09	143.60	7.24E-05	6.03E-05	1.78E-03	1.78E-03	3.08E-03	3.08E-03	1.63E-03	1.76E-03
30	18	3.57E-06	9.47E-09	220.43	6.50E-05	5.54E-05	1.65E-03	1.65E-03	2.83E-03	2.83E-03	1.55E-03	1.66E-03
40	24	4.73E-06	9.47E-09	292.37	6.06E-05	5.23E-05	1.64E-03	1.64E-03	2.79E-03	2.79E-03	1.49E-03	1.60E-03
50	30	6.02E-06	9.47E-09	371.57	5.71E-05	4.99E-05	1.56E-03	1.56E-03	2.65E-03	2.65E-03	1.45E-03	1.56E-03
60	36	7.24E-06	9.47E-09	447.26	5.45E-05	4.81E-05	1.54E-03	1.54E-03	2.56E-03	2.56E-03	1.41E-03	1.52E-03
70	42	8.49E-06	9.47E-09	524.54	5.24E-05	4.66E-05	1.51E-03	1.51E-03	2.53E-03	2.53E-03	1.39E-03	1.49E-03

Uncertainty Data for 100 psig system pressure:

VFD (%)	Freq. (Hz)	σ_Q (m^3/s)	σ_v (m^2/s)	σ_{Re} (-)	$\sigma_{f\text{-}Blasius}$ (-)	$\sigma_{f\text{-}CTF}$ (-)	$\sigma_{K\text{-}Blasius}$ (n=1)	$\sigma_{K\text{-}CTF}$ (n=1)	$\sigma_{K\text{-}Blasius}$ (n=6)	$\sigma_{K\text{-}CTF}$ (n=6)	$\sigma_{K\text{-}SG\text{-}1}$ (n=1)	$\sigma_{K\text{-}SG\text{-}3}$ (n=3)
10	6	1.13E-06	9.28E-07	71.11	8.63E-05	6.94E-05	2.02E-03	2.02E-03	3.59E-03	3.59E-03	1.79E-03	1.92E-03
20	12	2.33E-06	9.28E-07	146.84	7.20E-05	6.01E-05	1.78E-03	1.78E-03	3.03E-03	3.03E-03	1.63E-03	1.75E-03
30	18	3.54E-06	9.28E-07	223.02	6.48E-05	5.52E-05	1.66E-03	1.66E-03	2.84E-03	2.84E-03	1.55E-03	1.66E-03
40	24	4.78E-06	9.27E-07	301.41	6.01E-05	5.20E-05	1.60E-03	1.60E-03	2.69E-03	2.69E-03	1.49E-03	1.60E-03
50	30	6.03E-06	9.25E-07	381.45	5.67E-05	4.96E-05	1.55E-03	1.55E-03	2.59E-03	2.59E-03	1.44E-03	1.55E-03
60	36	7.19E-06	9.22E-07	456.32	5.42E-05	4.79E-05	1.56E-03	1.56E-03	2.59E-03	2.59E-03	1.41E-03	1.51E-03
70	42	8.45E-06	9.17E-07	538.76	5.20E-05	4.63E-05	1.51E-03	1.51E-03	2.53E-03	2.53E-03	1.38E-03	1.48E-03

Uncertainty Data for 150 psig system pressure:

VFD (%)	Freq. (Hz)	σ_Q (m^3/s)	σ_v (m^2/s)	σ_{Re} (-)	$\sigma_{f\text{-}Blasius}$ (-)	$\sigma_{f\text{-}CTF}$ (-)	$\sigma_{K\text{-}Blasius}$ (n=1)	$\sigma_{K\text{-}CTF}$ (n=1)	$\sigma_{K\text{-}Blasius}$ (n=6)	$\sigma_{K\text{-}CTF}$ (n=6)	$\sigma_{K\text{-}SG\text{-}1}$ (n=1)	$\sigma_{K\text{-}SG\text{-}3}$ (n=3)
10	6	1.09E-06	9.46E-07	67.11	8.76E-05	7.02E-05	2.20E-03	2.20E-03	3.93E-03	3.93E-03	1.80E-03	1.88E-03
20	12	2.49E-06	9.46E-07	154.09	7.11E-05	5.95E-05	1.54E-03	1.54E-03	2.63E-03	2.63E-03	1.62E-03	1.76E-03
30	18	3.58E-06	9.46E-07	221.18	6.50E-05	5.53E-05	1.62E-03	1.62E-03	2.77E-03	2.77E-03	1.55E-03	1.67E-03
40	24	4.90E-06	9.45E-07	303.01	6.01E-05	5.20E-05	1.50E-03	1.50E-03	2.55E-03	2.55E-03	1.49E-03	1.61E-03
50	30	6.01E-06	9.43E-07	372.66	5.70E-05	4.99E-05	1.54E-03	1.54E-03	2.59E-03	2.59E-03	1.45E-03	1.56E-03
60	36	7.34E-06	9.38E-07	457.30	5.42E-05	4.79E-05	1.46E-03	1.46E-03	2.46E-03	2.46E-03	1.41E-03	1.52E-03
70	42	8.46E-06	9.34E-07	529.81	5.22E-05	4.65E-05	1.49E-03	1.49E-03	2.49E-03	2.49E-03	1.38E-03	1.49E-03

Uncertainty Data for 200 psig system pressure:

VFD (%)	Freq. (Hz)	σ_Q (m^3/s)	σ_v (m^2/s)	σ_{Re} (-)	$\sigma_{f\text{-}Blasius}$ (-)	$\sigma_{f\text{-}CTF}$ (-)	$\sigma_{K\text{-}Blasius}$ (n=1)	$\sigma_{K\text{-}CTF}$ (n=1)	$\sigma_{K\text{-}Blasius}$ (n=6)	$\sigma_{K\text{-}CTF}$ (n=6)	$\sigma_{K\text{-}SG\text{-}1}$ (n=1)	$\sigma_{K\text{-}SG\text{-}3}$ (n=3)
10	6	1.08E-06	8.97E-07	70.70	8.64E-05	6.95E-05	2.12E-03	2.12E-03	3.93E-03	3.93E-03	1.79E-03	1.88E-03
20	12	2.62E-06	8.97E-07	170.60	6.93E-05	5.83E-05	1.37E-03	1.37E-03	2.36E-03	2.36E-03	1.60E-03	1.76E-03
30	18	3.55E-06	8.97E-07	231.20	6.43E-05	5.48E-05	1.64E-03	1.64E-03	2.80E-03	2.80E-03	1.54E-03	1.67E-03
40	24	4.78E-06	8.96E-07	311.70	5.96E-05	5.17E-05	1.57E-03	1.57E-03	2.66E-03	2.66E-03	1.48E-03	1.61E-03
50	30	6.04E-06	8.95E-07	394.73	5.62E-05	4.93E-05	1.52E-03	1.52E-03	2.55E-03	2.55E-03	1.44E-03	1.56E-03
60	36	7.38E-06	8.92E-07	483.58	5.34E-05	4.73E-05	1.44E-03	1.44E-03	2.41E-03	2.41E-03	1.40E-03	1.52E-03
70	42	8.58E-06	8.85E-07	566.58	5.14E-05	4.58E-05	1.44E-03	1.44E-03	2.41E-03	2.41E-03	1.37E-03	1.49E-03